Synthesis, catalytic activity, magnetic study and anticorrosive activity of mild steel in HCl 1 M medium of (H3dien)[Cu(NO3)(C2O4)2].2H2O. A redetermination at 100 K

Mohamed Akouibaa, Mariya Kadiri, Majid Driouch, Karim Tanji, Rachid Ouarsal, Souâd Rakib, Mouhcine Sfaira, Nicola Morley, Mohammed Lachkar, Brahim El Bali, et al.

To cite this version:

Mohamed Akouibaa, Mariya Kadiri, Majid Driouch, Karim Tanji, Rachid Ouarsal, et al.. Synthesis, catalytic activity, magnetic study and anticorrosive activity of mild steel in HCl 1 M medium of (H3dien)[Cu(NO3)(C2O4)2].2H2O. A redetermination at 100 K. Materials Chemistry and Physics, 2023, 307, pp.128130. ⟨10.1016/j.matchemphys.2023.128130⟩. ⟨hal-04393347⟩

HAL Id: hal-04393347
https://hal.science/hal-04393347v1

Submitted on 14 Jan 2024

Synthesis, catalytic activity, magnetic study and anticorrosive activity of mild steel in HCl 1 M medium of $(H_3dien)[Cu(NO_3)(C_2O_4)_2].2H_2O$. A redetermination at 100 K

Mohamed Akouibaa [1], Mariya Kadiri [2], Majid Driouch [2], Karim Tanji [3], Rachid Ouarsal [1], Souâd Rakib [1], Mouhcine Sfaira [2], Nicola Morley [4], Mohammed Lachkar [1,*], Brahim El Bali [5] Abdelkader Zarrouk [6,*] and El-Eulmi Bendeif [7]

[1] *Engineering Laboratory of Organometallic, Molecular Materials, and Environment (LIMOME), Faculty of Sciences, Sidi Mohamed Ben Abdellah University, 30000 Fez, Morocco*
[2] *Laboratory of Engineering, Modeling and Systems Analysis (LIMAS), Faculty of Sciences, Sidi Mohamed Ben Abdellah University, 30000, Fez, Morocco*
[3] *Independent Scientist, Fez, Morocco*
[4] *Department of Materials Science and Engineering, University of Sheffield, Sheffield S1 3JD, United Kindgdom*
[5] *Independent Scientist, Marrakech, Morocco*
[6] *Laboratory of Materials, Nanotechnology, and Environment, Faculty of Sciences, Mohammed V University in Rabat, Av. Ibn Battuta. P.O. Box 1014, Rabat, Morocco*
[7] *Université de Lorraine, CNRS, CRM^2, 54000 Nancy, France*

Corresponding author
Prof. Dr. Abdelkader Zarrouk
Email: azarrouk@gmail.com (AZ)
Scopus Author ID: 36125763200
https://orcid.org/0000-0002-5495-2125

Abstract

Diethylenetriammonium nitrato-bis(oxalato)cuprate (II) dihydrate $(H_3dien)[Cu(NO_3)(C_2O_4)_2].2H_2O$ (**1**) was synthesized by wet chemistry method. It was assessed for thermal stability (TG-DTA), single crystal X-ray diffraction, Fourier Transform Infrared spectroscopy (FTIR) and magnetic measurements. **1** crystallizes in the monoclinic system ($P2_1/c$), with the parameters: a= 10.1054(5) Å, b= 11.0825(5) Å, c= 14.8238(7) Å, β= 103.516(5)°, V= 1614.2 (1) Å^3 and Z= 4. The complex anions are distributed into layers, whilst the self-assembly of the inorganic-organic entities is assured by an intricate hydrogen network. At 413 K, the thermal behavior predominantly consists of the removal of water molecules, while its infrared spectrum displays distinct bands of oxalate, nitrate and diethylenetriamine groups. The catalytic test indicated that complex **1** exhibits a good catalytic activity in nitrophenol isomers (NP) reduction to aminophenols (AP). Moreover, **1** showed a high photocatalytic degradation efficiency 90% at 90 min toward the methylene blue (MB) dye under the UV irradiation. Due to the presence of the heteroatoms in its structure, the examined hybrid material's corrosion-inhibiting action in acidic conditions was more pronounced.

Keywords: Hybrid oxalate; Crystal structure; Spectroscopy; Photocatalysis; Corrosion.

1. Introduction

Investigation of novel inorganic-organic hybrid frameworks is one of the most active fields of materials science and chemical research. Considerable efforts have been devoted to the design of inorganic assemblies. Besides the mixed and hybrid networks, open-framework materials, like oxalates, chalcogenides, pnictides, cyanides, and thiopnictides, have been designed [1]. One emerging family of organic metal materials with open frameworks was reported in the last decade, and it includes metal oxalates that were widely synthesized and studied. Some divalent metals such as nickel [2-5], Copper [6], zinc [7-10] and cadmium [11-17], and trivalent metals such as indium [18] and neodymium [19] oxalates have also been reported. Thereby three-dimensional structures are formed if oxalate units connect the layers, others are layered oxalates with honeycomb networks and some of these structures are monomers. These materials have aroused a tremendous amount of interest in many applications, such as biology [20], catalysis [21, 22], electrical conductivity [23], ion-exchange processes [24], magnetism [25, 26], photomechanism [27] and separation [27, 28]. It has also been shown that these materials can be used in corrosion inhibition as an alternative to organic compounds [29-31]. Moreover, there were excellent results in using this type of materials as sorbents for dye removal [6]. The purpose of this work was to demonstrate the ability of a one-product of the copper oxalate family to be applied in several applications. Therefore, our research on copper oxalate complexes has led to the discovery of an open framework, copper oxalate dihydrate with the presence of organic amines and nitrate. The title compound has the general formula: $(H_3dien)[Cu(NO_3)(C_2O_4)_2].2H_2O$ with (dien=diethylenetriamine=($C_4H_{16}N_3$)), we hereby refer to it as “complex **1**”, or abstractly “**1**” . It is important to note that the crystal structure of this compound was already reported by Savel'eva et al. [32]. In this previous study carried out at room temperature, the authors observed a disorder on one of the oxygen atoms of the nitrate group with respective occupancies of 0.61 and 0.39 for the two sites. The accurate structural analysis we propose in this work was performed at low temperature (100 K) and shows no structural disorder. Moreover, the detailed description of the structural parameters discussed here would provide a better understanding of the physicochemical properties of this material. First, it was tested as a catalyst in the process of degradation of the three nitrophenol isomers (paranitrophenol (4-NP), metanitrophenol (3-NP), and orthonitrophenol (2-NP)) through sodium tetrahydroborate $NaBH_4$ to their corresponding aminophenol isomers (4-AP, 3-AP, 2-AP) that are less toxic. Second, **1** was tested in photocatalytic behavior versus photolysis effect (UV irradiation only) for methylene blue (MB) degradation. Finally, owing to the existence of heteroatoms in its structure that can be adsorbed on a metal surface in order to develop a layer that can hinder the contact between the metal surface and the corrosive electrolyte, complex **1** was applied to the corrosion inhibition of mild steel in 1 M HCl as acidic medium.

2. Experimental

2.1. Materials and instrumentation

All the chemicals and solvents used for the synthesis were of reagent grade quality and were obtained from commercial sources and used without further purification: $Cu(NO_3)_2.6H_2O$ (≥99.5%, Sigma-Aldrich), $H_2C_2O_4.2H_2O$ (≥99.5%, Sigma-Aldrich), Diethylenetriamine (≥ 98%, Sigma-Aldrich), 4-nitrophenol (≥ 99%, Sigma-Aldrich), 3-nitrophenol (≥ 99%, Sigma-Aldrich), 2-nitrophenol (≥ 99%, Sigma-Aldrich), $NaBH_4$ (≥ 96%, Sigma-Aldrich), Methylene Blue (≥ 85%, Sigma-Aldrich). The crystalline product was characterized by single-crystal X-ray diffraction analysis, Fourier Transform Infrared spectroscopy (FTIR), and thermal analysis. The single-crystal X-ray diffraction observations were performed at 100 K utilizing Mo-Kα radiation ($\lambda = 0.71093$ Å) and a 135 mm Atlas CCD detector on a SuperNova dual wavelength microfocus diffractometer. With a VERTEX 70 FTIR instrument (400-4000 cm^{-1}), the FTIR spectra were recorded using the ATR method with a resolution of 4 cm^{-1} at room temperature. TG analysis was carried out using a Diamond TGA/DTA equipment (Perkin-Elmer) thermal analyzer (25-800°C) in the air at a heating rate of 10 °C/min. The catalytic activity of $(H_3dien)[Cu(NO_3)(C_2O_4)_2].2H_2O$ in the reduction of the three nitrophenol isomers (2-NP, 3-NP, and 4-NP) to their corresponding aminophenols was assessed using a Camspec M550 double beam scanning UV-Visible spectrophotometer.

2.2. Synthesis of $(H_3dien)[Cu(NO_3)(C_2O_4)_2].2H_2O$

Single crystals were obtained by a slow evaporation technique. An amount of $Cu(NO_3)_2.6H_2O$ (0.34 g, 1.41 mmol) and dihydrate oxalic acid $H_2C_2O_4.2H_2O$ (0.52 g, 2.82 mmol) were dissolved in distilled water (20 mL). A quantity of diethylenetriamine ($C_4H_{16}N_3$) (1.50 mL, 13.81 mmol) was added dropwise to the blue solution (20 mL) of copper (II) nitrate hexahydrate. The resulting light blue solution became dark blue (pH = 5) after the addition of diethylenetriamine. The mixture was stirred at room temperature for two hours, then was filtered and allowed to evaporate at room temperature. Three weeks later, we had hexagon-shaped blue single crystals that were dried in the air after being cleaned in cold water and 80% ethanol. The crystals are insoluble in water and ethanol. The crystals were found to be air stable. The initial characterization was performed using infrared (IR) and thermogravimetric analysis (TGA).

2.3. Single crystal study

For X-ray diffraction examination, a suitable crystal with the dimensions of 0.13×0.13×0.12 mm^3 was selected. The *CrysAlis* program suite was used for the unit cell determination, data collection and reduction, and analytical absorption corrections [33]. The crystal structure was determined using direct methods and serial Fourier difference syntheses, and, then, it was refined using the SHELX suite's weighted full-matrix least squares method against F2 [34]. The corresponding structure is monoclinic and is described in the $P2_1/c$ space group. The non-hydrogen atoms were refined in anisotropic approximation. The differential density allowed for easy identification of each H atom. Fourier maps' atomic coordinates and isotropic displacement parameters were altered utilizing the appropriate restraints, particularly for those associated with water molecules and ammonium groups. All calculations were carried out using the WinGX software package [35]. The DIAMOND program was used to draw the structural graphics [36]. Main crystallographic data, data collecting and structure refinement information are summarized in Table 1. Tables 2 and 3 present basic geometrical information and atomic coordinates, respectively, while Table 4 presents hydrogen bonding. The Cambridge Structural database has the cif-file for the investigated chemical listed as CCDC 2168015. On request to the Director, CCDC, 12 Union Road, Cambridge CB2 1EZ, UK, fax: +44 (0)1223 336033, or email: deposit@ccdc.cam.ac.uk, copies of the material are accessible free of charge.

2.4. Magnetization and a.c. susceptibility measurements

The magnetic properties as a function of temperature and magnetic field were measured using a Quantum Design MPMS-3 device. The magnetization *vs*. field loops were measured at 2 K and 300 K, to a field of 2 T. Field cooled (FC) and zero field cooled (ZFC) between 2 K and 350 K, measurements of a.c. susceptibility and d.c. magnetization were made with an applied field of 100 Oe. At each temperature, the a.c. susceptibility measurements were taken at three applied frequencies: 10, 100 and 1000 Hz.

2.5. Reduction process of nitrophenol isomers

The reduction of the three-nitrophenol isomers (4-nitrophenol, 3-nitrophenol, and 2-nitrophenol) to aminophenol isomers was used to assess the complex's catalytic activity (4-aminophenol, 3-aminophenol, and 2-aminophenol). Using a Camspec M550 double beam scanning UV-visible spectrophotometer, the concentration fluctuations of the three-nitrophenol isomers during their catalytic transformation in the presence of the complex were monitored. In fact, a conventional test involved mixing (40 mL) of a 4×10^{-4} M aqueous solution of one of the three isomers of nitrophenol, such as 2-nitrophenol, 3-nitrophenol, or 4-nitrophenol, with (40 mL) of an 8×10^{-4} M aqueous solution of sodium tetrahydroborate ($NaBH_4$) while stirring continuously at room temperature. After commencing the reaction without a catalyst, the color of the solution abruptly changes to a dark yellow tint as a result of the creation of the nitrophenolate ion. At the same time, an absorption peaks were observed at 401, 393 and 415 nm for 4-nitrophenol, 3-nitrophenol and 2-nitrophenol, respectively. Complex **1** (0.05 g) was then added to the aqueous solution under continuous stirring, and it is resulted in the disappearance of the dark yellow color of the solution under the effect of the catalyst. This reduction reaction was monitored via UV-Vis spectra measurements.

2.6. Photocatalytic experience for Methylene Blue degradation

The tests were carried out in a batch reactor (100 mL) for 120 min, first without light for 30 min, and then with a 300 W Osram Ultra-Vitalux lamp fitted with an Edmund Optics polyester UV filter sheet that exhibits 99.9% absorption below 390 nm. The reuse catalyst tests were performed by using the same catalyst sample during four cycles. After each cycle (30 min), the $(H_3dien)[Cu(NO_3)(C_2O_4)_2].2H_2O$ particles were washed and dried at 90°C and the MB solution volumes were modulated to keep constant the catalyst/dye ratio (1 g/L). The concentration of MB solution was evaluated by spectrophotometric analysis at λmax= 664 nm using an J.P. SELECTA, S.A. VR-2000 spectrophotometer and the degradation efficiency was calculated using the following Equation (1):

$$Degradation\,(\%) = \frac{C_0 - C_t}{C_0} \times 100 \qquad (1)$$

where C_0 and C_t are the initial concentration (t=0) and the measured concentration at $t \neq 0$ of MB solution.

2.7. Electrochemical measurement

Working electrodes were made of mild steel (MS), which had the following chemical composition: ≈ 0.3700% C, ≈ 0.2300% Si, ≈ 0.6800% Mn, ≈ 0.0160% S, ≈ 0.0770% Cr, ≈ 0.0110% Ti, ≈ 0.0590% Ni, ≈ 0.0090% Co, ≈ 0.1600% Cu, and the remaining iron (Fe). The surface of MS was polished using grit emery papers from 100 to 2000. The inhibitor molecule under study was dissolved in an aggressive solution of 1 M HCl prepared by dilution of concentrated acid, which had a density of d = 1.19 and 35% in mass. The concentration range used varies from 1×10^{-3} to 1×10^{-6} M. Platinum grid and second kind electrode of Ag/AgCl, 3 M KCl were used as auxiliary and reference electrodes, respectively.

The electrochemical survey data were collected through the Bio-Logic device type sp150 implemented with EC-Lab software. The explored techniques were non-destructive such as linear polarization resistance (LPR) and electrochemical impedance spectroscopy (EIS). For LPR measurement, the potential was swept from -25 mV to +25 mV versus the open circuit potential E_{OCP}, with a scan rate of 0.166 mV/s. In the case of the EIS technique, the frequency range was suitable for determining the steady state response of the systems under test ranging from 100 kHz to 100 mHz with low amplitude of perturbation of 10 mV. The steady state of the system is obtained after immersion of the working electrode in the tested solutions during 30 min under controlled temperature of 298 K.

3. Results and discussion

3.1. Description of the structure

The crystal structure of the title complex $(C_4H_{16}N_3)[Cu(NO_3)(C_2O_4)_2].2H_2O$ was previously studied by Savel'eva and co-workers [32]. In their study carried out at room temperature, they observed a disorder of one of the oxygen atoms of the nitrate group with respective occupancies of 0.61 and 0.39 for the two sites. In order to better understand the origin of this disorder (static or dynamic), we performed a structural analysis at low temperature (100 K). The low temperature structure does not show any disorder and thus reveals that the one observed at 298 K is dynamic. The molecular structure can be described as being composed of $[Ni(C_2O_4)_2(NO_3)]^{3-}$ anions, $(C_4H_{16}N_3)^{3+}$ cations and two crystallization water molecules, linked by means of electrostatic interactions and an extensive network of hydrogen bonds. The asymmetric unit contains 26 atoms other than hydrogen (Figure 1).

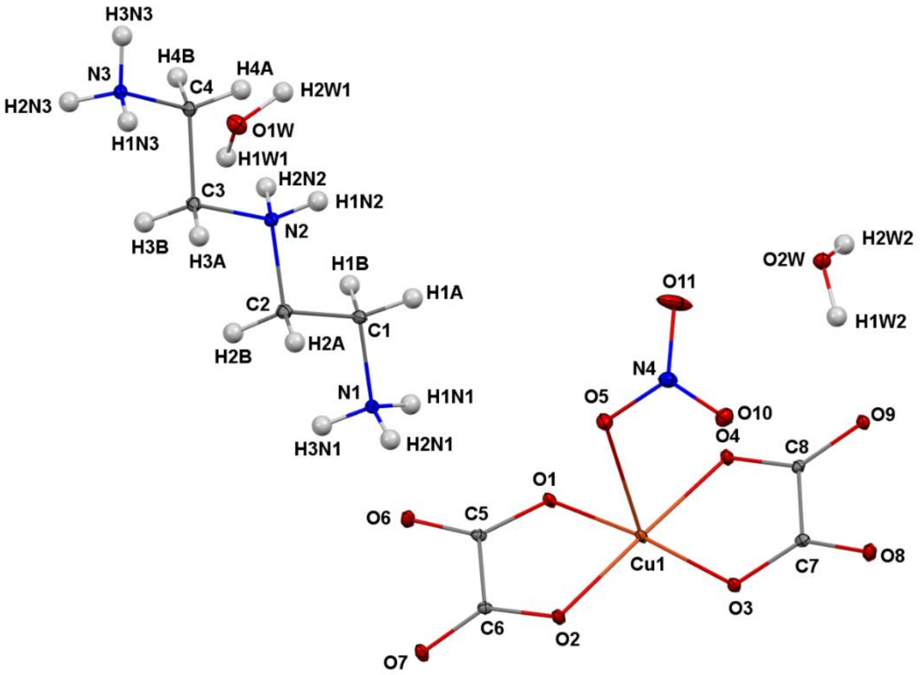

Figure 1: The asymmetric unit of $(C_4H_{16}N_3)[Cu(NO_3)(C_2O_4)_2].2H_2O$.

The Cu(II) ion is chelated by two oxalate bidentate ligands through the couplings (O1, O2, and (O3, O4) and one nitrate monodentate via the O5 oxygen atom, leading in the $[Cu(C_2O_4)_2(NO_3)]$ (dsp^3 hybridization) square pyramidal unit, as seen in Figure 1. The O3-Cu-O1 and O4-Cu-O2 angles surrounding the Cu^{2+} ion are significantly deformed and they are equal to 172.77° and 178.39° respectively (Table 3). On the other hand, by means of the following equation $\Delta_{oct} = 1/6\times\Sigma[(d_i\text{-}d_m)/d_m]^2$ [37,38], the bond-length distortion for the octahedron is 2.4×10^{-2}, greater than 2.6×10^{-3} found in the isostructural compound $(H_3dien)[Ni(NO_3)(C_2O_4)_2].2H_2O$ [39]. In fact, O1 from the nearby $[Cu(C_2O_4)_2(NO_3)]$ unit, which is located at a distance of 2.815(1) Å, is the closest non-bonded oxygen atom, and it is also contributing to the coordination of Cu through the Jahn-Teller effect as a waited for divalent Cu^{2+} in the electronic configuration $3d^9$. It results, thus, in the transition from square pyramid (dsp^3 hybridization) into the distorted octahedron (sp^3d^2 hybridization), giving rise to dimmers (Figure 2), which interact in the structure through a network of H-bonds of the organic amine and water molecules (Figure 3, Table 3). Consequently, the crystal structure of Complex 1 might be seen as a 3D network made of dimmers $[Cu(NO_3)(C_2O_4)_2]$~2~ interacting via H-bonds interactions through the organic part of the structure, as shown in Figure 3. The dimmers are, however, isolated in the structure, with the shortest distance Cu…Cu of 3.6151(4) Å, which is comparable with the distance Ni…Ni = 3.6070(3) Å found in $(H_3dien)[Ni(NO_3)(C_2O_4)_2].2H_2O$ [39].

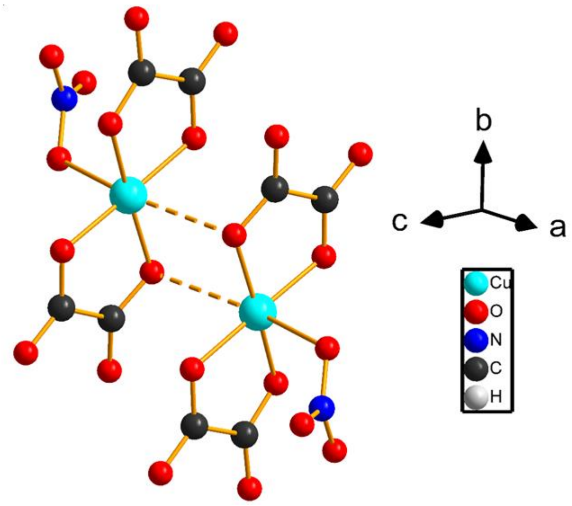

Figure 2: A dimer in the crystal structure of $(C_4H_{16}N_3)[Cu(NO_3)(C_2O_4)_2].2H_2O$.

The bond lengths in the triprotonated $(H_3dien)^{3+}$ cation is in good agreement with the literature data for related compounds containing such a cation [39, 40]. The Cu-O(ox) (oxalate) bond distances are in the range of 1.9424(8)-1.9497(8) Å. The O-Cu-O angles are in the range of 85.25-97.33° with an average value of 91.52° (Table 3). These values are similar to those found in a chain compound $H_2[Cu_2(bpy)_2(H_2O)_2(\mu\text{-ox})]_2[H_2W_{12}O_{40}].9H_2O$ [41]. The Cu-O(5) (nitrate) bond length of 2.4229(9) Å is comparable with its homologous in $[Cu(C_{12}H_8N_2)](NO_3)_2$ [42]. One, nevertheless, can note that this bond is longer than that found in $[Cu(NO_3)(C_{12}H_8N_2)_2]NO_3.C_7H_6O_5.H_2O$ [43] and is shorter than that reported for the complex $[Cu_2(Bipy)_2(H_2O)_2(C_2O_4)(NO_3)_2]$ [44]. We also observe that the C—O bond lengths in the (ox)-ligands are different for coordinated and non-coordinated oxygen atoms. Indeed, the distances observed for the coordinated oxygen atoms (O1, O2, O3 and O4) are in the range of 1.274(1)-1.285(1) Å, while those of uncoordinated oxygen (O6, O7, O8 and O9) vary from 1.234(1) to 1.241(1) Å. The N—O bond lengths in the NO_3 group are varying from 1.232(2) to 1.273(1) Å and the O–N–O angles are typically of 120°. These geometrical parameters are consistent with the values reported in $[Cu(H_2O)_2(C_{12}H_8N_2)(NO_3)]NO_3$ [45]. The average values of the C—C and C—N bond lengths are 1.534(2) and 1.487(1) Å, respectively. In addition, the O-C-O and O-C-C angles are equal to 125.91 and 116.81°, respectively. In addition, the O–C–O and O–C–C angles are respectively of 125.91° and 116.81°. These values are in good agreement with the expected values, as reported by Audebrand and her coworkers for oxalate compounds [46].

The three-dimensional crystal packing of **1** is built of molecular species interconnected by strong O—H···O implicating the water molecules and the nitrate group, and moderate N-H···O hydrogen bonds involving the oxalate ligands and $(H_3dien)^{3+}$ cations. The three-dimensional network is also characterized by the presence of weak C-H···O intermolecular interactions (**Table 4**). It is noteworthy that the behaviour of the oxygen atoms of the oxalate groups coordinating the copper metal centre are different. The O1 atom is not involved in the hydrogen bonding networks, whereas O2 only participates in one N—H...O hydrogen bond and O3 and O4 are involved in one weak C-H···O intermolecular interactions. The other four oxygen atoms of the oxalate groups (O6, O7, O8 and O9) acts as a bifurcated acceptor through N-H···O hydrogen bonds with the ammonium groups of different $(H_3dien)^{3+}$ cations. It should be noted that these interactions were also observed in the crystal packing of the structure determined at 298 K. However, we note a slight strengthening of all the interactions and more particularly (~ 2%) of the interactions observed between the water molecule and the nitrate group (O1W-H2W1···O5) and the one involving the ammonium group and the O9 oxygen atom of the oxalate ligand.

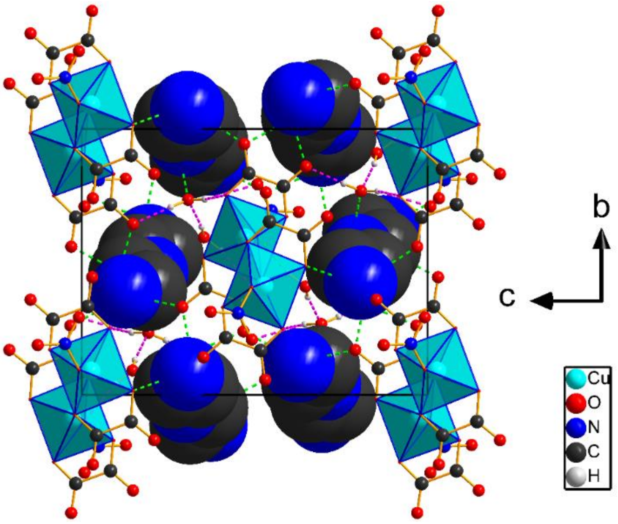

Figure 3: Perspective view of the structure of $(C_4H_{16}N_3)[Cu(NO_3)(C_2O_4)_2].2H_2O$ along the *a*-axis, H-bonds as dashed lines: pink (O…H-O), green (O…H-N).

3.2. Magnetic properties

Temperature and magnetic field were used to measure the sample's magnetic response. It is observed in Figure 4 that the d.c. magnetization response and the a.c. magnetization response has the same behavior with temperature. There are no peaks detected over the temperature range, and no difference in behavior is observed between the zero-field-cooled and the field-cooled behaviors. In relation to temperature, the response is typical of a paramagnetic material. Ethe equation can be used to calculate the sample's Curie constant from these data $C = \frac{MT}{H}$, taking H= 100 Oe, and fitting the equation to the d.c magnetization data, gives a Curie Constant, C= 0.465 emu.K/mol.Oe. At 2 K and 300 K, the magnetization was also measured in relation to the magnetic field. It is observed that there is a linear response with an applied field, which would be expected for a paramagnetic material. Again, the Curie constant can be determined using the above equation, at 300 K, and it gives C = 0.461 emu.K/mol.Oe, which is in good agreement with the other measurement. Thus, the average Curie constant from these two measurements is 0.463 emu.K/mol.Oe.

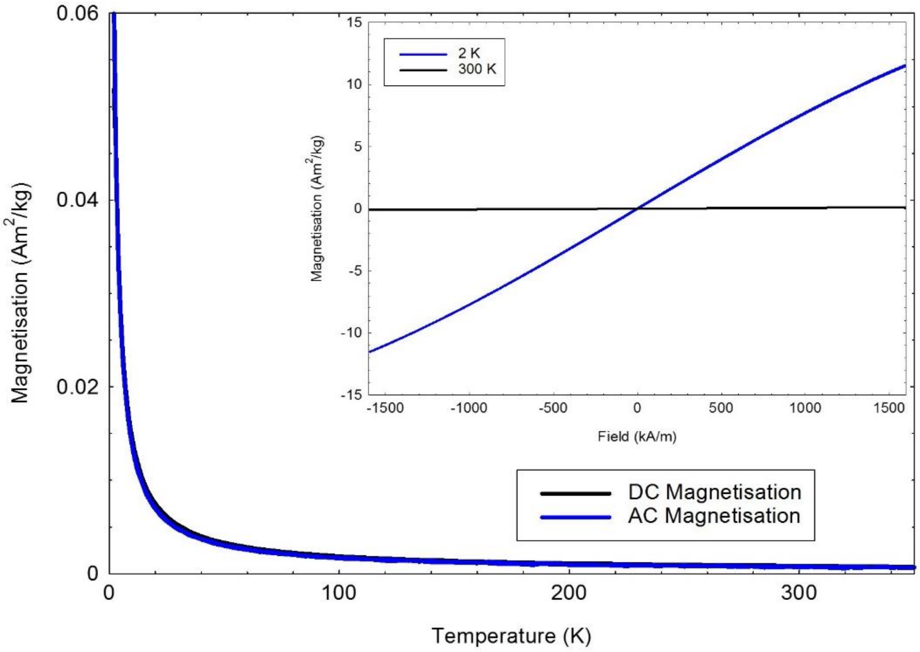

Figure 4: d.c. and a.c. magnetization as a function of magnetic field taken at 100 Oe and 100 Hz for the a.c. magnetization data. The solid line represents the zero field cooled data and the dashed line represents the field cooled data. Inset: Magnetization as a function of magnetic field and temperature.

Additionally, the a.c. susceptibility was assessed in relation to temperature and a.c. frequency (Figure 5). It is observed that, for the real susceptibility component, there is no difference between the different applied frequencies. The behavior observed is common for a paramagnet, as no peaks or differences in the zero-field cooled and field-cooled data are observed. To determine whether the sample has a magnetic transition below 2 K and to determine the Curie constant again, the following equation was fitted to the data:

$$\chi = \chi_0 + \frac{C}{T+\theta} \qquad (2)$$

where χ_o is the temperature independent susceptibility, C is the Curie constant and θ is the Curie-Weiss temperature. The values measured were χ_o = 8.35 x 10^{-4} emu/Oe/mol, C = 0.429 emu.K/mol.Oe and θ= 0.256 K. Thus, there is good agreement between the different measurements of the Curie constant. The Curie-Weiss temperature is much lower than 2 K, meaning that the sample will show paramagnetic behaviour for temperatures above 1 K. Another parameter that can be derived from the real component of the a.c. susceptibility is the effective moment, and it can be obtained using the equation: $\mu_{eff} = 2.82\sqrt{\chi T}$. For this sample the μ_{eff} is 2.35 μ_B, which is slightly higher than the expected effective moment of Cu^{2+} ions of 2.2 μ_B, but this is often observed in paramagnet samples.

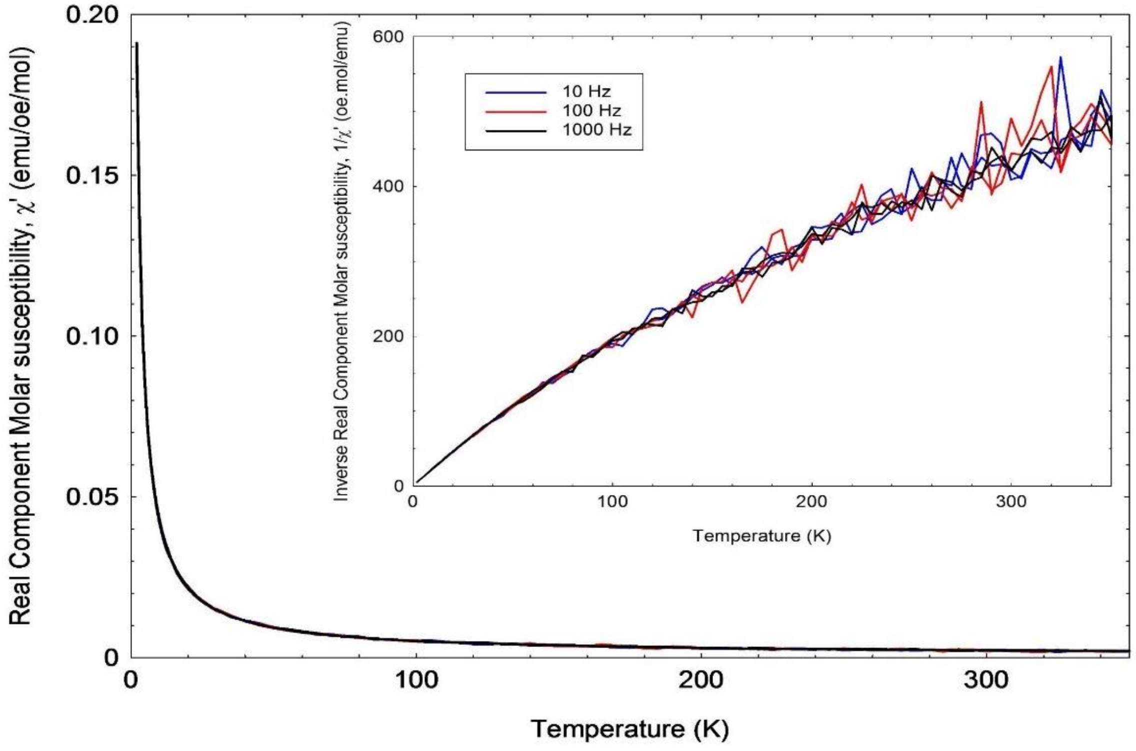

Figure 5: Real a.c. susceptibility component as a function of temperature and frequency at a 100 Oe applied field Inset. At an applied field of 100 Oe, the inverse real component of the a.c. susceptibility was studied as a function of temperature and frequency.

3.3. Infrared spectroscopy

We looked into the vibrational characteristics of compound **1** to provide more details on the crystal structure. The presence of oxalate group, organic amine cations, water molecules, and different types of nitrate group coordination were all identified using infrared spectroscopy. The designated infrared bands for complex **1** are listed in Table 5. The diethylenetriammonium cation (H_3dien), nitrate anion, water, and oxalate groups can all be seen in the infrared spectrum of complex **1** as having different vibrational modes (Figure 6). There are two significant bands present in the FT-IR spectrum, with wavenumbers between 3215-2642 cm^{-1} and 1708-1511 cm^{-1}. The deconvolution technique offers a thorough band-based interpretation. In line with the structure determined by single crystal X-ray structure, the FT-IR spectrum does in fact show that the molecule contains all of the functional groups. Even if it is challenging to assign each band in detail, the most crucial attribution mode is obtained by comparison with comparable and related chemicals reported in the literature [47, 48]. The principal bands are assigned to the internal modes of organic cation. The presence of the diethylenetriamine group in the product is confirmed by the clearly visible vibration bands of -CH_2-, -NH_2, C-N, and -NH that belong to the diethylenetriammonium cation. The vibration band of C-N at 1137 cm^{-1} is pushed toward a lower wavenumber (1060 cm^{-1}), while the -NH band, pointing at 890 cm^{-1} and 669 cm^{-1}, has changed and is now nearly invisible when compared with the IR spectrum of pure diethylenetriamine [49-52]. In fact, the frequency region of 3600-3215 cm^{-1} is related to the symmetric, asymmetric stretching vibrations of NH_2 and OH of the diethylenetriammonium and water molecules forming the hydrate [53, 54]. The intense bands observed at 2824 and 2941 cm^{-1} are assigned to (-CH_2) vibrations.

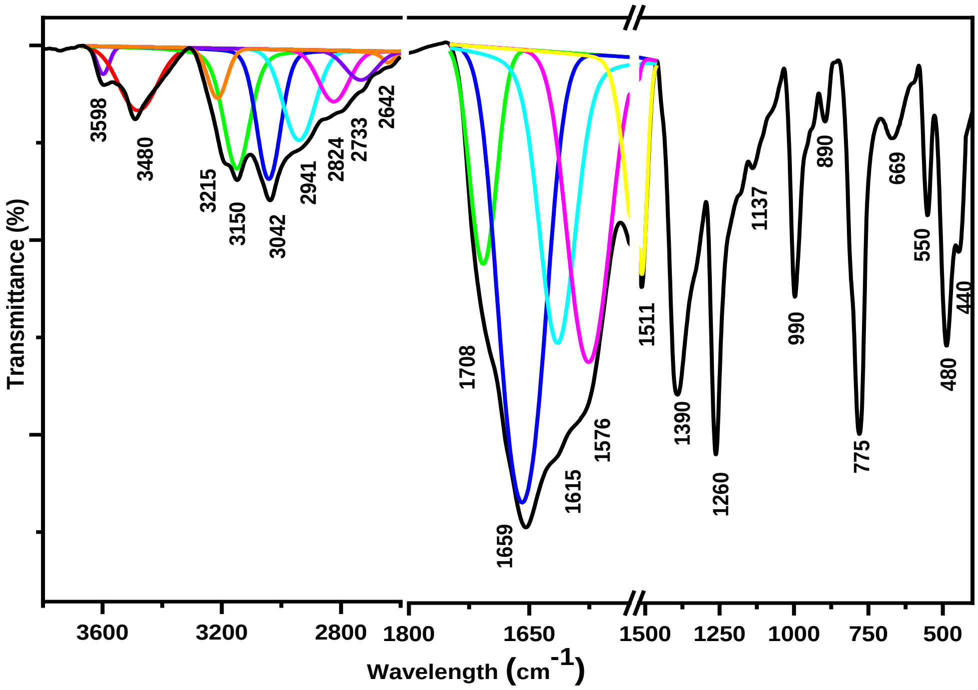

Figure 6: Infrared spectrum of $(C_4H_{16}N_3)[Cu(NO_3)(C_2O_4)_2].2H_2O$.

The characteristic absorption bands of the oxalate $C_2O_4^{2-}$ groups are found at 1708, 1659 cm^{-1} [$\nu_{as}(CO_2)$], 1615, 1511 cm^{-1} [$\nu_s(CO_2)$], and bending vibration of carboxylic groups at 775 cm^{-1} [$\delta(CO_2)$], respectively [55-57]. Comparing with that of oxalic acid dihydrate ($H_2C_2O_4{\cdot}2H_2O$), the asymmetric stretching vibration of carboxylic groups $\nu_{as}(CO_2^-)$ has a shift of about 20 cm^{-1}. The main and possible reason may be related to the deprotonation of the oxalic group due to the fact that the Cu(II) cation forms stronger coordination interactions with the oxygen atoms of the oxalic acid. Nitrate within a complex material is characterized by the presence of several modes of coordination; the symmetrical or asymmetrical monodentate and bidentate chelate modes, as well as the bridging bidentate ligand. Vibrational spectroscopy can be used to discriminate between these modes. They vary slightly in terms of nitrate anions' symmetry (C_{2v} or C_s) [58-61]. When the nitrate ion functions as a monodentate coordinating agent (C_{2v} symmetry), according to Gatehouse et al., all bands become active [62], and three bands corresponding to the stretching vibration mode are observed as expected for its C_{2v} symmetry mode. Therefore, the infrared spectrum of complex **1** shows three bands corresponding to the nitrate group. The asymmetric stretching $\upsilon_{as}(NO_2)$ nitrate group vibration is observed as the band at 1390 cm^{-1}, and the symmetric stretching $\upsilon_s(NO_2)$ vibration is observed at 1260 cm^{-1} [63, 64]. The N-O stretching vibration of the coordinated nitrate group (NO) is found to be at 990 cm^{-1} as expected for its C_{2v} symmetry [65]. The bands observed at 550 and 480 cm^{-1} are related to the elongation mode of Cu-O. The absorption bands assigned in the infrared spectrum of copper complex are in agreement with those of complexes previously considered in the literature [66, 67].

Table 5

Infrared bands and assignments for $(C_4H_{16}N_3)[Cu(NO_3)(C_2O_4)_2].2H_2O$.

Bands (cm^{-1})	Assignment
3598	$\nu_{as}(H_2O)$
3480	$\nu_s(H_2O)$
3215	$\nu_{as}(-NH_2)$
3125	ν_s $(–NH_2)$
3042	$\nu_{as}(NH_3^+)$
2824 and 2941	$\nu_s(-CH_2)$
1708 and 1659	$\nu_{as}(O-C-O)$
1615	$\delta(H_2O)$
1576	$\delta_{as}(-NH_2)$
1511	$\nu_{as}(NO_2)$
1390	$\nu_s(O-C-O)$
1260	$\nu_s(NO_2)$
1137	$\delta(NH_3^+)$
1117	$\nu(-CN)$
1196	$\nu(-C-C)$
990	Coordinated nitrato group
890 and 669	$\nu(-NH)$
775	$\delta_{as}(O-C-O)$
540 and 480	$\nu(Cu-O)$

3.4. Thermal analysis (TGA/DTA)

Thermogravimetry (TG) measurements were carried out in dynamic air using a Diamond instrument (Perkin-Elmer) thermal analyzer. The treatment of this compound was realized in the flowing air (Debit = 50 mL/min) in the temperature range of 25-800°C (scan rate = 10°C/min), as shown in Figure 7. The powdered sample was spread evenly in a large crucible to prevent the mass effect. The TG/ATD curve of the title compound can be divided into a four-step mass loss stage. The first weight loss (seen at 8.5%, calculated at 8.11%) is associated with the endothermic dehydration of two water molecules at 140°C. This is referring to the tenuous hydrogen connection that keeps water within the structure of crystals. The loss of organic amine ($C_4H_{13}N_3$), the release of CO_2, and NO_2 relates to oxidative degradation of the of organic amine and nitrate ions (seen 60.5%; calculated 62.7% weight loss) associated with the second stage decomposition occurs in the temperature range of 150-310°C and is seen with an endothermic process. The next step following continuous two-step weight loss is related to the decomposition of $2CO_2$ gas with exothermic flux in the temperature range of 320-550°C which accounts for 19.23% weight loss (calculated = 19.82% weight loss). The corresponding mass loss of 15% agrees well with that expected upon the formation of CuO. The following reactions were used to compute these weight losses, which mostly related to the breakdown of organic amine and nitrate groups:

$$(C_4H_{16}N_3)[Cu(NO_3)(C_2O_4)_2].2H_2O \xrightarrow{140^\circ C\,(endo)} (C_4H_{16}N_3)[Cu(NO_3)(C_2O_4)_2] + 2H_2O$$

$$(C_4H_{16}N_3)[Cu(NO_3)(C_2O_4)_2] \xrightarrow{150-310^\circ C\,(endo)} Cu(C_2O_4) + C_4H_{16}N_3 + NO_2 + 1/2O_2 + 2CO_2$$

$$Cu(C_2O_4) \xrightarrow{320-350^\circ C\,(exo)} CuCO_3 + CO$$

$$CuCO_3 \xrightarrow{400-600^\circ C\,(exo)} CuO + CO_2$$

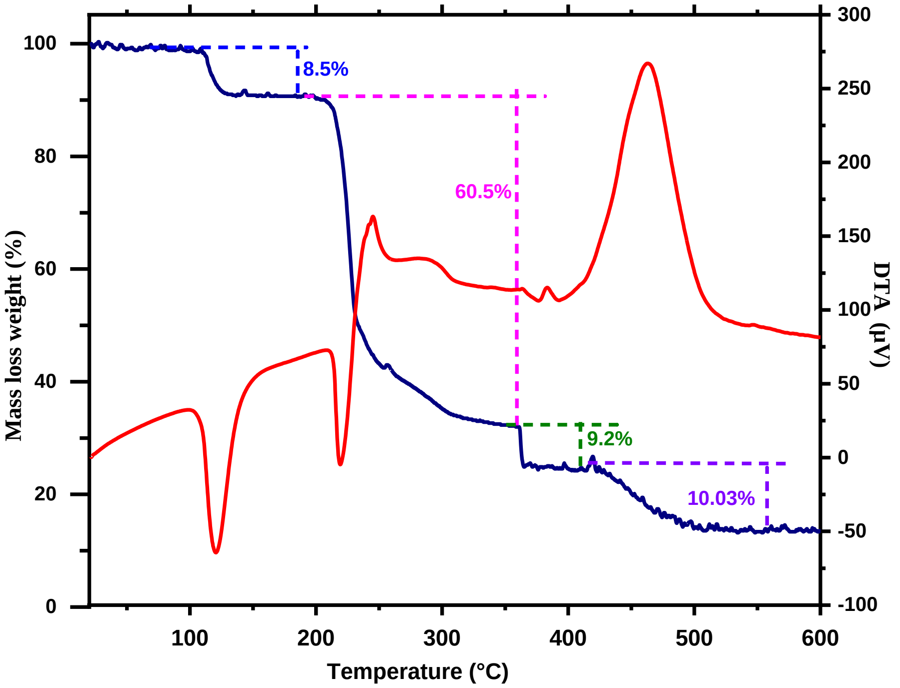

Figure 7: TGA-DTA analyses of $(C_4H_{16}N_3)[Cu(NO_3)(C_2O_4)_2].2H_2O$.

3.5. Determination of catalytic reduction of nitrophenol isomers

The reduction process of nitrophenol isomers to aminophenol isomers using sodium tetrahydroborate at room temperature was used to test the material's catalytic activity. In fact, a quick and intense coloring of the solution was seen after adding $NaBH_4$; this was caused by the formation of phenolate anions, and the liquid supernatant was examined using a UV-Visible spectrophotometer at 400 nm. This training is consistent with the deprotonation of the nitrophenol isomers, and $NaBH_4$ had no effect on the decrease. In outline, the as-prepared catalyst (0.05 g) was introduced into 40 mL of nitrophenol (NP) aqueous solution (1 M) and 40 mL of $NaBH_4$ as a reducing agent (aqueous solution 1 M) and the results are plotted in Figure 8(a), (b), and (c). After 10 s of starting the reaction, the solution becomes uncolored and complex **1** was found to be very efficient as a catalyst. The higher absorption bands vanish, giving way to new bands at 347, 328, and 317 nm, which correspond to 4-NP, 3-NP, and 2-NP, respectively. These new bands were assigned to the presence of the respective aminophenol (AP) isomers. At ambient temperature, the reaction was completed within 30 s for 2-NP and 3-

NP, and within 60 s for 4-NP. This result shows excellent catalyst efficiency, and the complex can be considered a promising candidate for the reduction of the nitrophenol function. A comparison of the catalyst with complex **1** and other materials reported in the literature is given in Table 6.

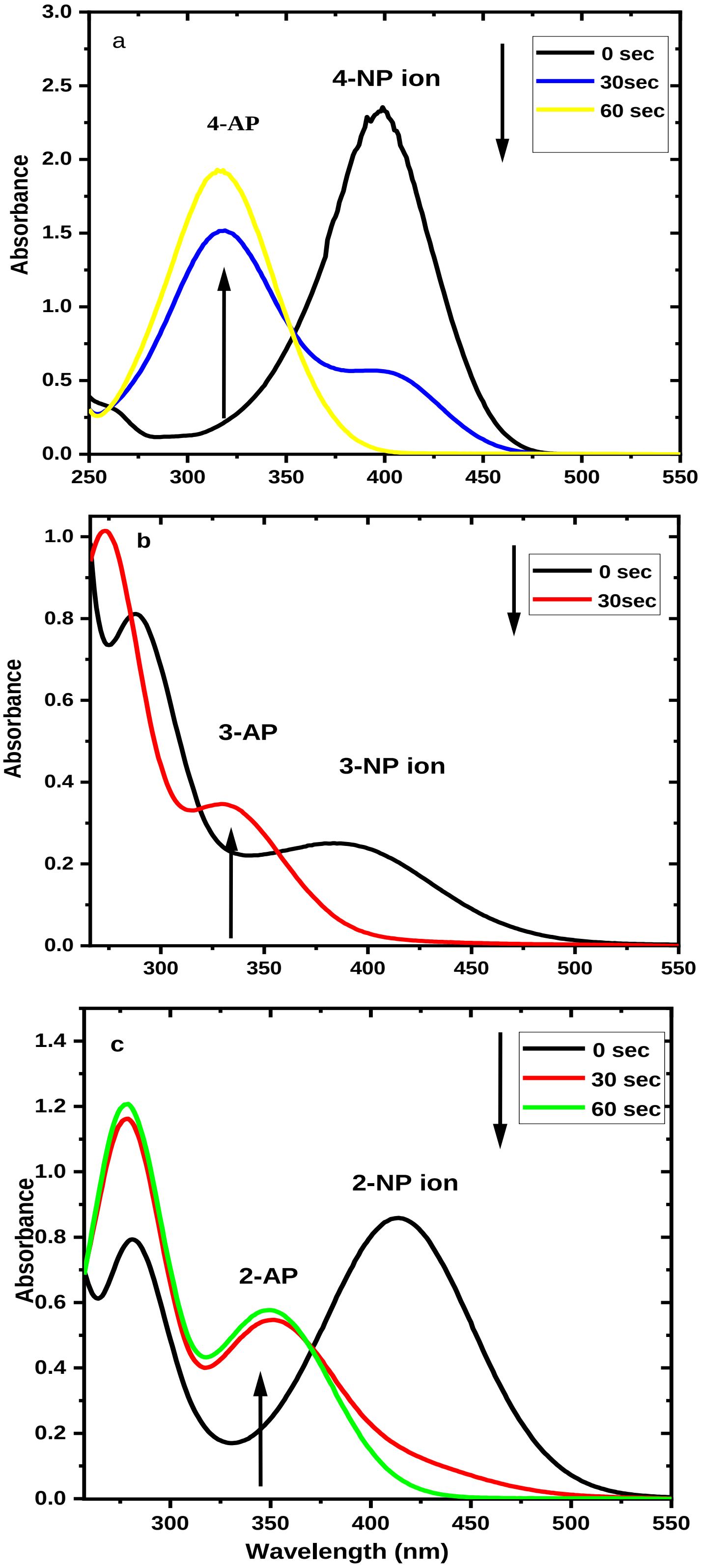

Figure 8: At room temperature, the UV-visible spectra of the following isomers were measured in the existence of sodium tetrahydroborate and after the addition of compound **1**. a, b, and c are (4-NP), (3-NP), and (2-NP), respectively.

Table 6

Comparison of the reaction time of the reducing activity of complex **1** with known catalysts.

Catalyst	Concentration of NP (mol/L)	Reaction Time (s)	Reference
$(H_3dien)[Cu(NO_3)(C_2O_4)_2].2H_2O$	4×10^{-4}	60 for 4-NP 30 for 3-NP 60 for 2-NP	This work
$(H_3dien)[Ni(NO_3)(C_2O_4)_2].2H_2O$	4×10^{-4}	30 for 4-NP 30 for 3-NP 30 for 2-NP	[39]
$(C_4H_{12}N_2)[Co(H_2O)_6](HPO_4)_2$	4×10^{-4}	240 for 4-NP 30 for 3-NP 240 for 2-NP	[68]
$CuMoO_4$	4×10^{-4}	840 for 4-NP 360 for 3-NP 840 for 2-NP	[69]

3.6. Photocatalytic activity of the hybrid oxalate

Figure 9 reports the results of the photocatalytic behavior of **1** compared to the photolysis effect (UV irradiation only) for the degradation of MB. In the presence of $(H_3dien)[Cu(NO_3)(C_2O_4)_2].2H_2O$ particles, the photolysis has almost no effect on the MB degradation (2% during 120 min). Moreover, the results showed that the adsorption phenomenon was insignificant for **1** that reached only 12%, thereafter the MB removal was rapidly enhanced to achieve 90% at 90 min under the UV irradiation, and it confirms the photocatalytic behavior of the title complex.

Eventually, $\ln(C/C_0)$ versus contact time for **1** is given in Figure 10. Thereby, assuming the first-order reaction, the kinetic constant was calculated using Equation (3) and found to be kc = 0.021 ± 0.001 min^{-1}.

$$\ln\frac{C_0}{C_t} = K_c \Delta t \qquad (3)$$

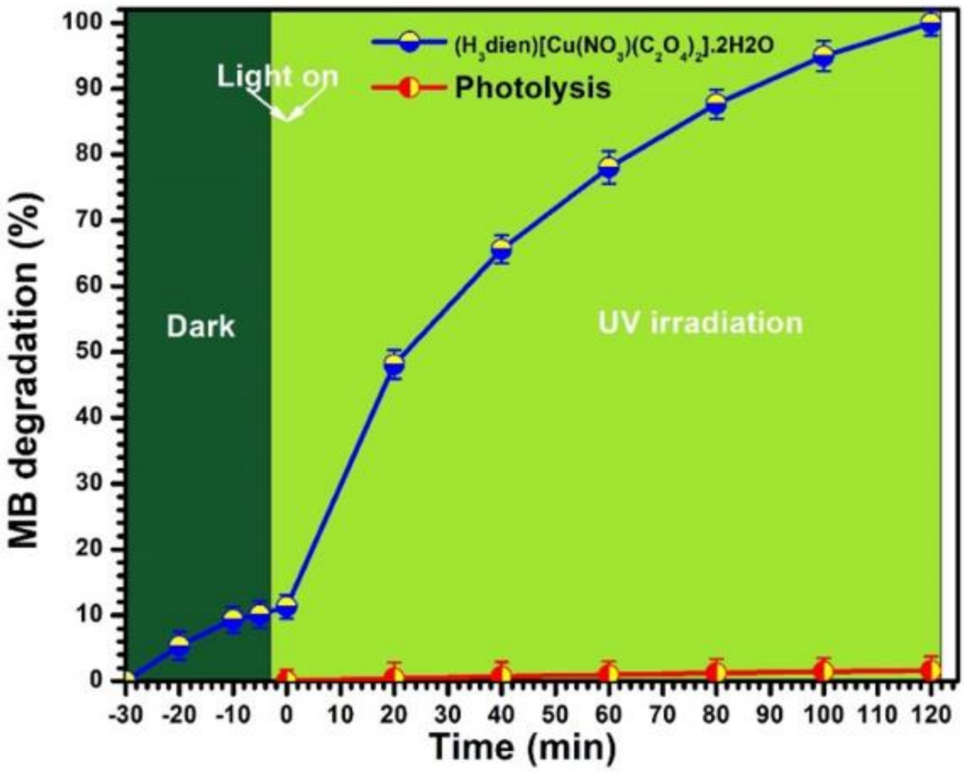

Figure 9: The photodegradation of MB under UV illumination using 1 g/L of **1**, [MB] = 20 ppm, pHi = 5 and T = 25 ± 3°C.

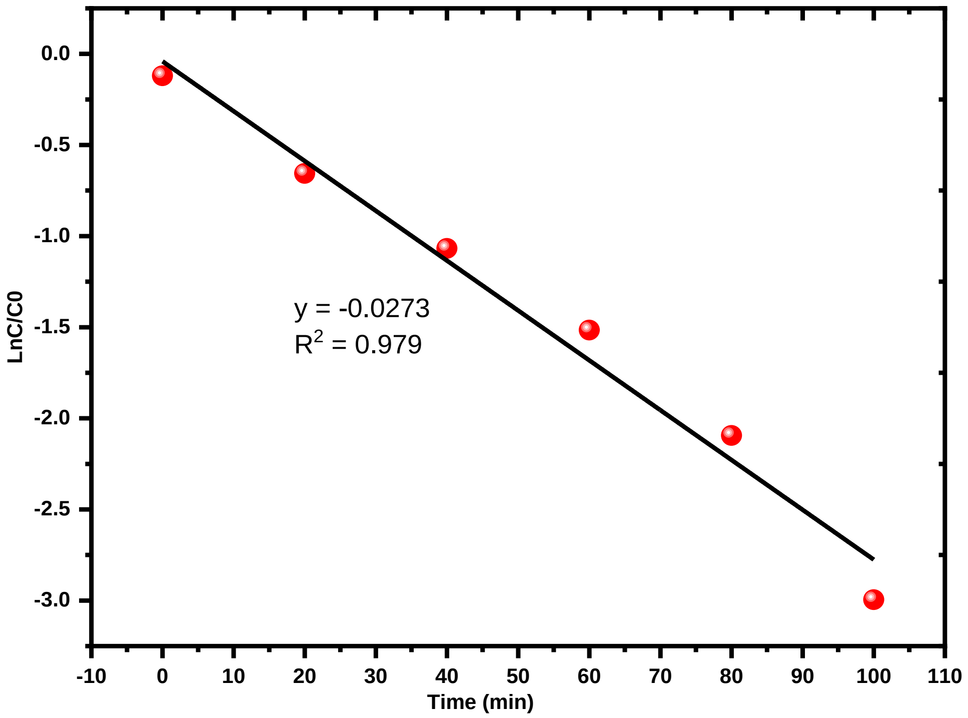

Figure 10: The kinetic of MB photodegradation using $(C_4H_{16}N_3)[Cu(NO_3)(C_2O_4)_2].2H_2O$.

For future large-scale applications, the investigation of the stability and recyclability of the photocatalyst is considered as very essential. Hence, four cycles of catalyst recovery and reuse were performed using 1 g/L of **1** and [MB]= 20 ppm at room temperature and the achieved results displayed in Figure 11 exhibited a decrease of photodegradation efficiency after each cycle that reached 84% after the fourth use. Indeed, a photocatalytic activity reduction of 16% after four reuse cycles could be explained by the residual MB adsorbed on the photocatalyst that influences the degradation process in the next cycle [70].

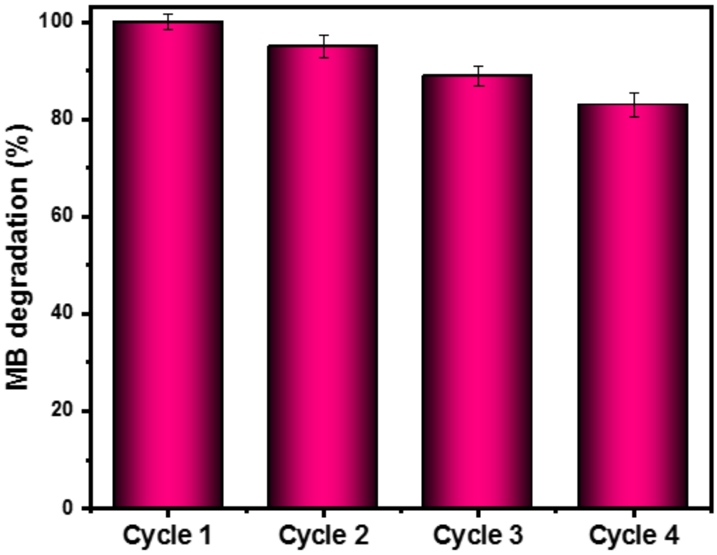

Figure 11: Decolorization efficiency through four consecutive reuse cycles.

The alteration of plant growth is one of the wastewater effects, and, thereby, the test of seed germination and their root elongation is one of the simplest and short-term methods that generally indicates the toxicity of polluted water [71, 72]. Hence, to investigate the toxicity of MB solution before and after treatment, a corn kernel germination test was carried out. Figure 12 exhibits the images of Petri dishes containing corn kernels immersed in the same volume of 20 ppm of MB solution (A), MB solution after photodegradation using 1 g/L of **1**, [MB]=20 ppm, pH=5.9 and room temperature (B), and distilled water (C) and the results of germination rate versus germination days (D).

As noticed in Figures 12.A and 12.D, the germination rate of the seeds immersed in the untreated MB solution was very low and did not exceed 20% on the sixth day (Figure 12.A). However, it reached 100% for the treated MB solution with significant root growth (Figure 12.B-D), similarly, the results of seeds soaked in distilled water indicate complete germination and remarkable root elongation for six days (Figure 12.C). These findings prove the high efficiency of **1** for the degradation of MB and promise future applications for the treatment of real wastewater that could be reused for irrigation.

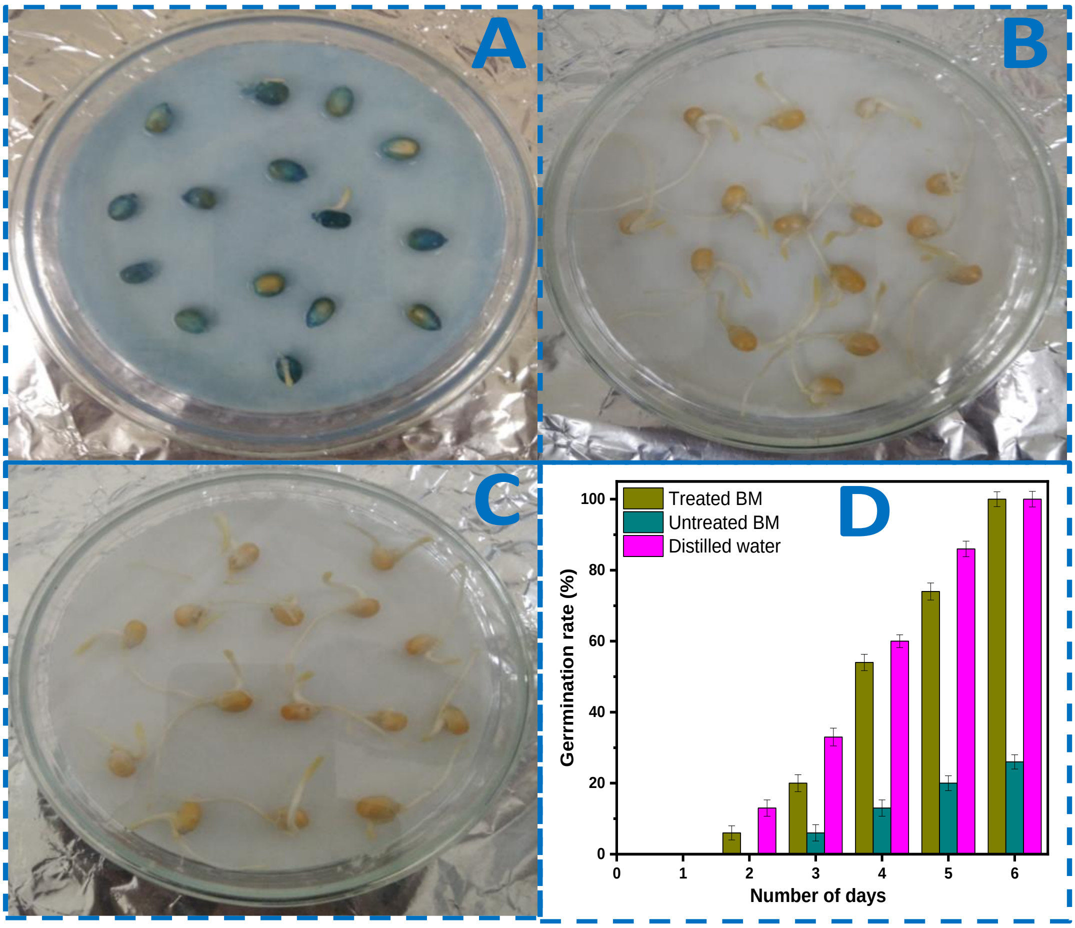

Figure 12: Germination of corn kernels in MB solution (A), degraded MB (B), distilled water (C) and (D) graph of germination rate (%).

3.7. Electrochemical measurement

3.7.1. LPR measurement

The current density-potential curves have been considered as one of the most applied studies initially to determine the mechanism and the kinetics of the corrosion reaction. It is possible to exploit these curves differently to determine their components and that LPR is one of these methods; or called Stern & Geary method. Its principle, introduced by Wagner and Traud [73], was applied by Bonhoeffer [74] and deeply discussed by Stern and Geary [75]. The range of potential used to disrupt the system is from -25 mV to +25 mV around the corrosion potential E_{corr}. The typical curves obtained after immersion of MS in the corrosive solutions in the presence and absence of compound **1** at 298 K are shown in Figure 13.

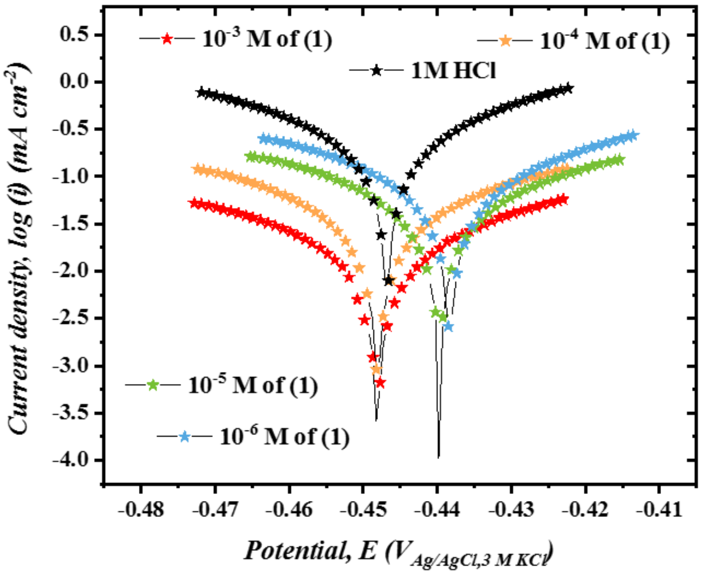

Figure 13: Polarization curves in potential range ± 25 mV in the presence and absence of **1**.

It can be concluded from Figure 13 that both iron dissolution, taking place at the anodic sites, and cathodic hydrogen evolution reactions are inhibited after the addition of **1** in 1 M HCl solution. All curves in the existence of the inhibitor are consequently lower than the curve of the unfettered solution. Complex **1** is inhibiting these processes to a greater extent at concentrations between 1×10^{-6} and 1×10^{-3} mol. L^{-1}. However, there is no clear trend in the shift of E_{corr} values at different concentrations of compound **1** [76,77].

The data presented in Figure 14, by applying the linear regression method, indicate the linear relation between the current and potential. The slope of this straight line has a unit of resistance given by the following Equation (4):

$$R_p = \frac{\Delta E}{\Delta i} = \frac{\beta_a \beta_c}{2.303 i_{corr} (\beta_a + \beta_c)} = \frac{A}{2.303 i_{corr}} \qquad (4)$$

where β_a and β_c are the slope of Tafel, i_{corr} is the corrosion current. The equation of the straight lines shown in Figure 14 is written as follows (Equation 5):

$$E = E_{corr} + \left(R_p \times i\right) \qquad (5)$$

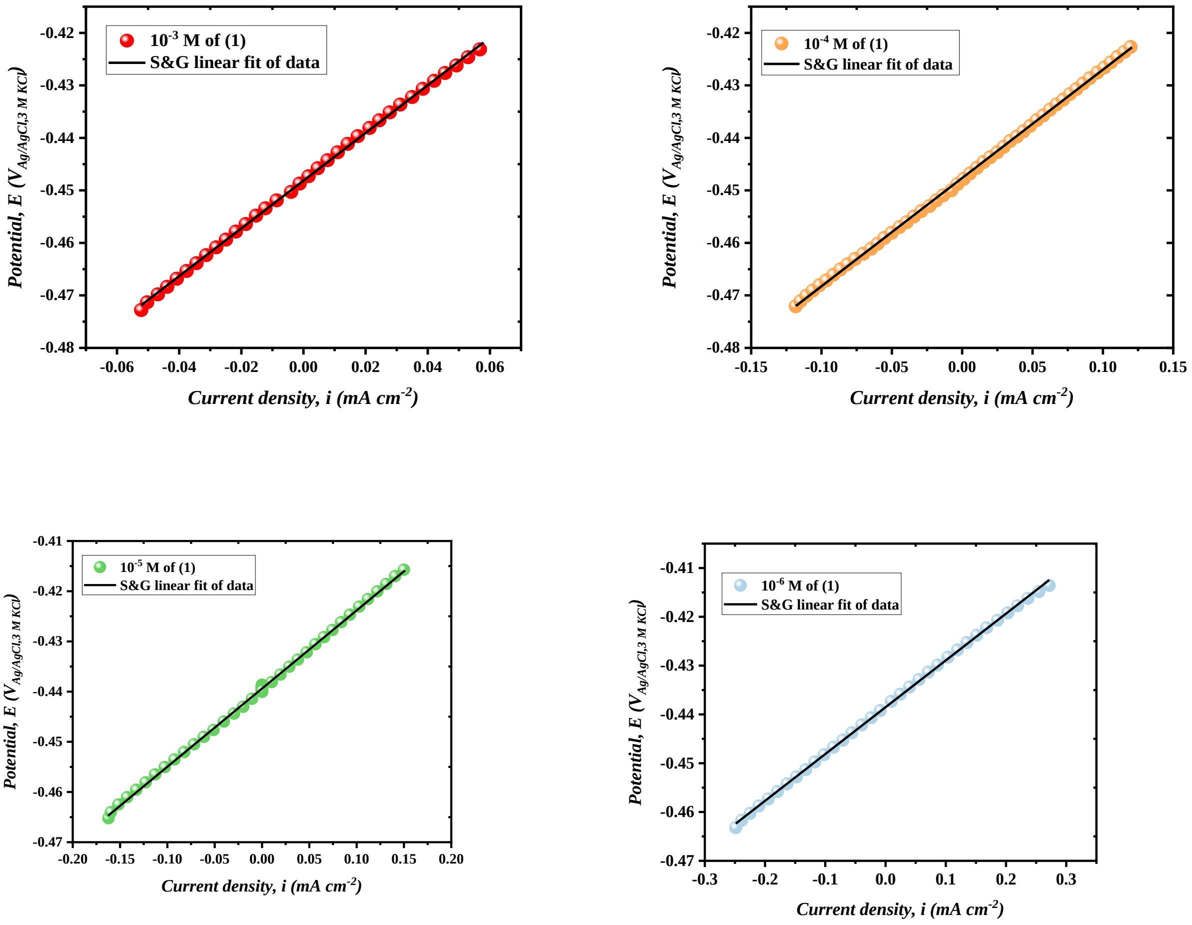

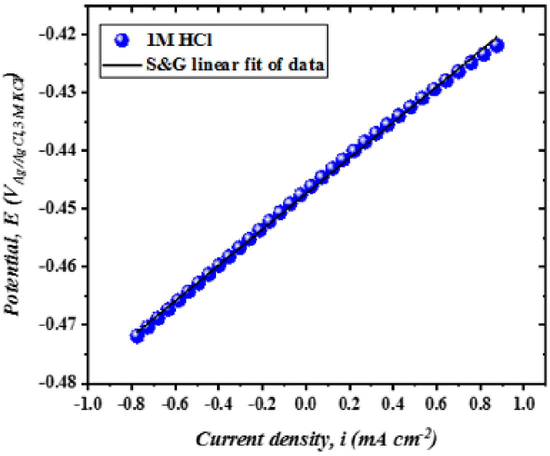

Figure 14: Linear polarization resistance of MS/1M HCl + {C_i mol L^{-1} of complex **1**}.

The extracted parameters from the linear regression of the slope, such as E_{corr}, R_p and correlation coefficient are regrouped in Table 7. Also, the inhibiting efficiency is evaluated upon Equation (6):

$$\eta_{S\&G}(\%) = \left(\frac{R_{p/inh} - R_p}{R_{p/inh}}\right) \times 100 \qquad (6)$$

R_p and $R_{p/inh}$, the resistance of MS in the solution without and with complex **1**, respectively.

As seen in equation (6), the LPR method only yielded the value of R_p; however, the constant A's value is still unknown and necessitates the use of another method, such as the Tafel curves. Because the system under research must be polarized over a large range of potentials and currents in order to obtain Tafel lines, the Tafel method was not used in this study. In cathodic polarization, the film developed at the surface could be reduced, and this leads to generation of an additional current. Upon anodic reaction, at high anodic polarization the molecules of the inhibitor are desorbed, widely discussed in the literature under the name of desorption potential E_d, which attributes a change of the surface state by dissolving the metal in the solution and consequently the composition of the solution is changed. Since only the area close to the open circuit potential E_{ocp} is of relevance, the linear polarization resistance technique avoids the majority of the issues caused by broad polarization. For this reason, the values of R_p reported in Table 7 are intended to reflect the inhibiting efficiency of these molecules [78].

It is obvious that, the domain of linearity is well and truly verified. Therefore, it was found that the polarization resistance of the MS and the resulting inhibiting efficiency increased with **1**´s concentration rise, and reached a value of 92.59% at 1×10^{-3} mol. L^{-1}. This behavior is due to the adsorption of the organic molecules of the inhibitor on the metal surface. Also, the presence of copper atoms in the structure of $(C_4H_{16}N_3)[Cu(NO_3)(C_2O_4)_2].2H_2O$ has a significant influence on the formation of a stable and persistent film thus decreasing the corrosion rate by blocking the anodic and/or cathodic sites associated with the metal dissolution and proton reduction reactions in solution [30].

Table 7

Parameters derived from S&G method.

Mild steel/1M HCl + {C_i mol L^{-1} of 1}	0	1×10^{-6}	1×10^{-5}	1×10^{-4}	1×10^{-3}
E_{corr} {$mV_{Ag/AgCl,3M\ KCl}$}	-447.35	-438.52	-439.39	-447.63	-448.14
R_p {Ω cm^2}	30.73	95.91	155.72	206.20	455.52
η_{SIE} {%}	-	67.95	80.26	85.09	92.59
R^2	0.999	0.999	0.998	0.999	0.999

3.7.2. Electrochemical impedance spectroscopy measurement

It is not surprising that electrochemical techniques are used extensively in the study of corrosion phenomena to ascertain the corrosion rate and define the degradation mechanisms because partial corrosion reactions, such as metal oxidation and hydrogen reduction, are charge transfer processes. As a result, EIS looks to be the most useful method since it can identify interfacial relaxations across a variety of relaxation periods in a single experiment. The principle of this technique is to stimulus a low amplitude alternating potential signal to measure the electric field or current difference generated between different active sites of the metal surface. For this reason, EIS measurement is used to gather more information of the interface MS/**1** + 1M HCl at 298 K. The results obtained are plotted in both Nyquist and Bode representations (Figure 15), profiting from the complementarity of the two plots.

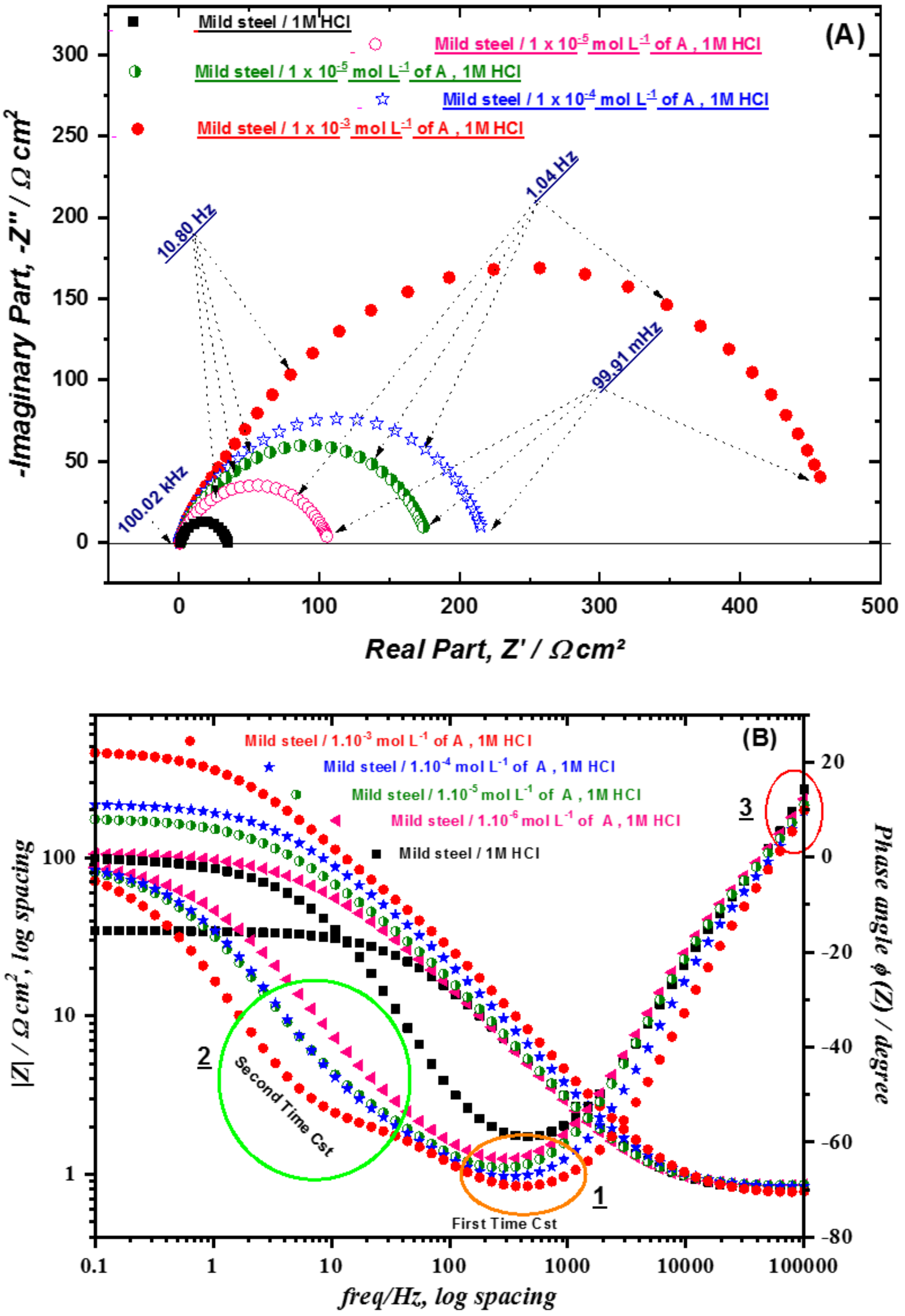

Figure 15: MS Nyquist & Bode graphs in 1 M HCl without and with varying concentrations of **1** at 298 K.

The recorded EIS measurements of the interface MS/**1** in 1M HCl show that the impedance response is a depressed semicircle below the X abscissa, which represents the real part axis *(Z')* in the Nyquist plot (Figure 15.A). The spectra confirm that the response of the interface depends on the disturbance frequency, generate a phase shift between an applied alternating potential and its current response. This phase shift called constant phase element (CPE) is recently widely treated in the literature [79, 80]. This behavior of frequency dispersion at the interface is generally attributed to heterogeneity of the surface [80, 81]. The impedance of CPE is described by Equation (7):

$$Z_{CPE} = \frac{1}{Q(j\omega)^n} \qquad (7)$$

Indeed, the diameter of these loops increase with rising concentration of **1** attributed to a greater coverage of the active sites by molecules of complex **1**. These first visual examinations lead to the proposal of a first equivalent electrical circuit (EEC) with one time constant for modeling these spectra represented by Equation (8) depicted in Figure 16.A:

$$Z(\omega) = R_1 + \frac{1}{\frac{1}{R_2} + Q(j\omega)^n} \qquad (8)$$

R_1 represent the solution resistance, R_2 refer to resistance of polarization [82]. Finally, Q is the parameter of CPE and n is the constant phase exponent ($0 < n < 1$) related to the deviation of the straight capacitive line from 90° by an angle α given by Equation (9):

$$\alpha = 90° \, (1 - n) \qquad (9)$$

($j^2 = -1$) is the imaginary number and ω is the angular frequency.

The Bode representation, which plot the phase angle and the modulus of impedance versus frequency, exploits the advantage offered by the frequency dependence of the representation, which allows to distinguish the different reaction stages displayed at the interface. As illustrated in Figure 15.B, that the plot of the phase angle as a function of frequency (Φ(Z) *vs* logf) characterized by two minima neatly distinguished [83]. The first one appears at high frequencies part numbered (1) and the other one is located at low frequencies part numbered (2) in Figure 15.B. It should be noted that this second minimum appears only after the addition of **1** in the corrosive solution compared to inhibited solution (1M HCl). This result is consistent with the fact that the corrosion inhibition process in this case is carried out upon two stages with two-time constants leading to separate the processes of the double layer charging and of the adsorption of the **1** at the MS surface [84]. Thus, the EEC with one time constant previously suggested is inappropriate to simulate the experimental data in the presence of inhibitor.

Further, the modulus of (Z) versus frequency (log|Z| vs. logf) is useful to quickly assessing the presence of resistive components (flat with frequency), and capacitive components (decreasing with increasing frequency). Accordingly, an EEC with two-time constants was used to fit the obtained data. After testing several circuits, the most appropriate circuit found and offering meaningful results is that reported in Figure 16.B.

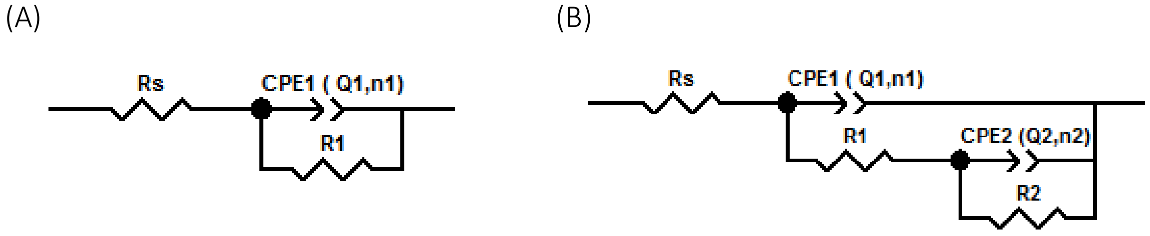

Figure 16: Equivalent electrical circuit models {EEC}.

Before interpreting the generated parameters derived from the impedance diagrams, a detailed illustration can be found in Figure 17, describing the goodness of fit of the experimental data by the two circuits suggested before. Hence, the following EEC ($R_S+CPE_1/[R_1+CPE_2/R_2]$) simulates well the obtained results shown by a good superposition between experimental and fitting data. In contrast, the circuit with one-time constant ($R_S+ CPE_1/R_1$), which exhibits a poor fit of the spectra, remains an adequate circuit to model the interface MS/1M HCl alone.

The attribution of the two-time constants to the electrochemical processes taking place at the interface MS/1M HCl + complex **1**, is based on a good understanding of the studied system as well as, not only the appropriate choice of the electric equivalent circuits, but also the evaluation of the parameters resulting from the simulation led to make an attribution which be correlated to the response of the interface. Consequently, the first time constant, that appears at high frequencies range resulting from a kinetically fast phenomenon, is generally attributed to the relaxation of the double layer and charge transfer process, followed by a kinetically slow process assigned to the resistive-capacitive response of the film developed onto the metal surface due to the adsorption of molecules **1** [85].

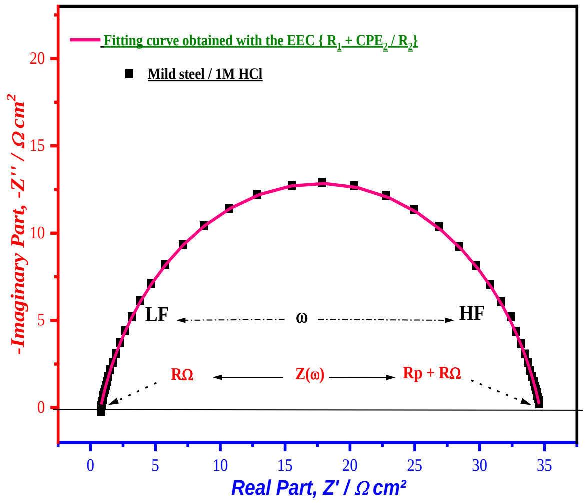

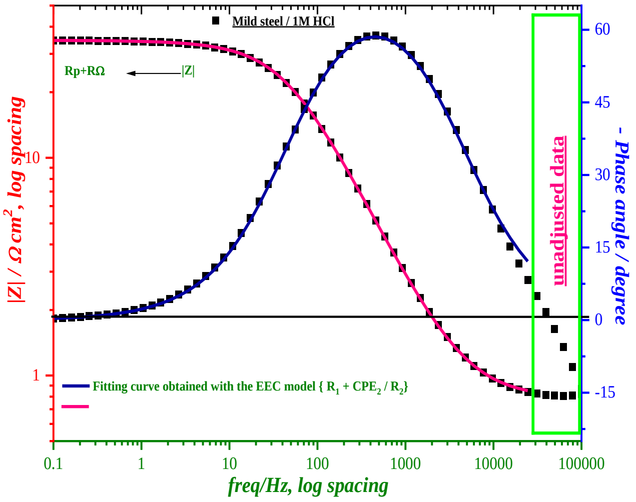

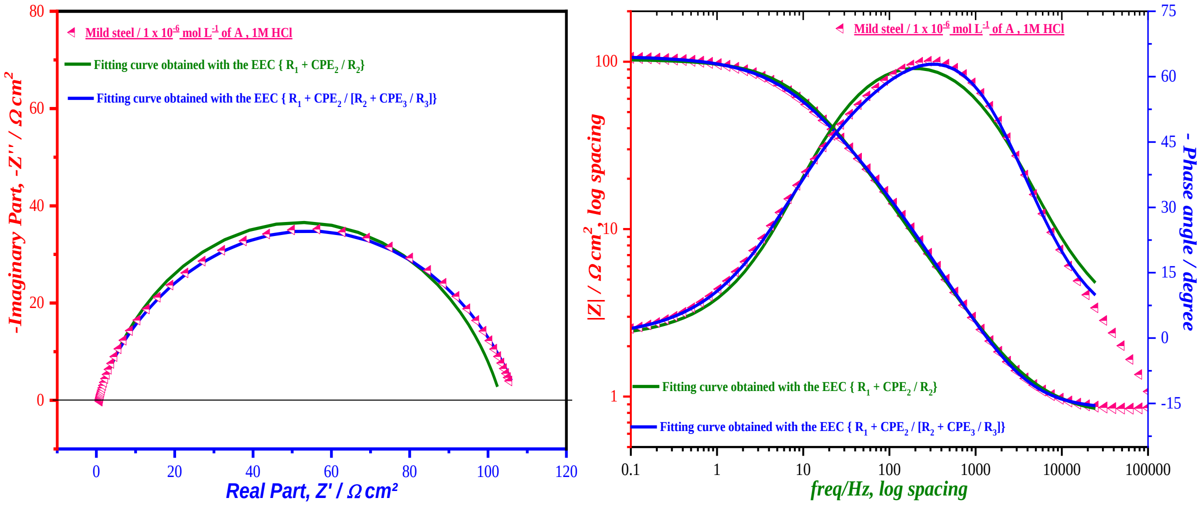

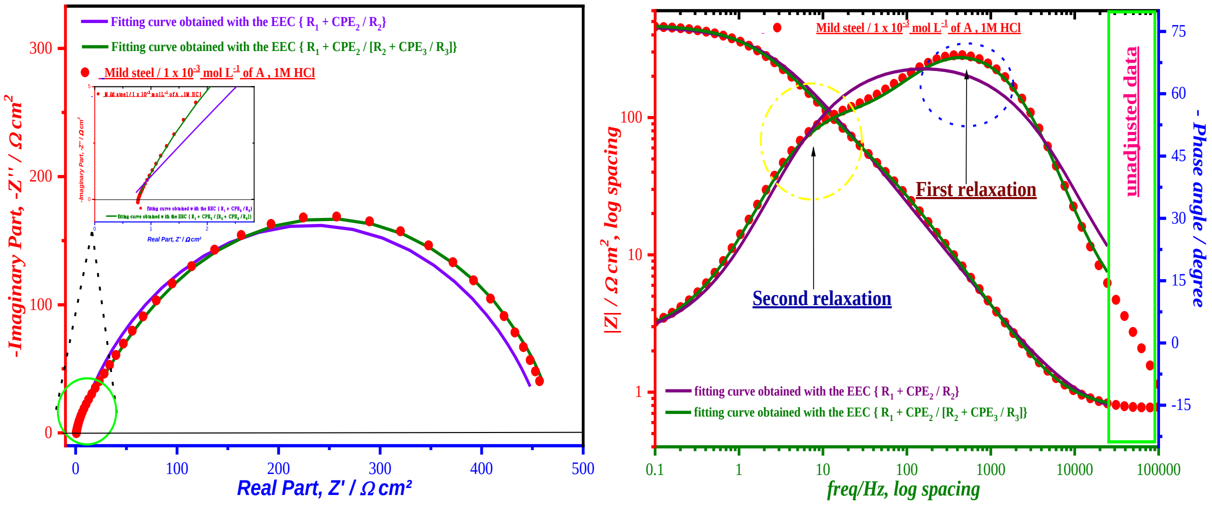

Figure 17: Nyquist and Bode diagrams simulated by $\{R_s+CPE_{dl}/R_{ct}\}$ and $\{R_s+CPE_{dl}/(R_{ct}+CPE_f/R_f)\}$ at different concentrations of complex **1**.

The electrochemical characteristics of the system MS/1M HCl in the presence and absence of **1** are compiled in Table 8. Also, the inhibiting efficiency calculated by equation (6) where R_p is derived from results of EIS study by Equation (10):

$$R_P = R_{ct} + R_f \qquad (10)$$

It is seen from Table 8 that the value of R_{ct} increases with rising of inhibitor concentration [86]. The value of the parameter of CPE (Q_{dl}) varies regularly so as to follow a decreasing trend is observed as the concentration rises. Thus, the value of n_{dl} grows as well (0.82-0.87), when compared to that obtained in solution of 1M HCl alone. This can be attributed to a certain decrease of the initial surface inhomogeneity resulting from the adsorption of **1** on the most active sites [87]. Also, these results could be confirmed by the values of R_f that gets enhanced from 74.24 Ω cm^2 at concentration of 10^{-6} mol L^{-1} to 395.20 Ω cm^2 at the maximum concentration of 10^{-3} mol L^{-1}, so adsorption of **1** is proved, although at lower concentrations. Consequently, R_f dominates the calculated polarisation resistance R_P. The value of Q_f along with that of n_f show the same trend as the parameters of Q_{dl} indicating the enhancement at the surface of the MS and the uniformity of the developed film due to the adsorption of **1** at the anodic as well as the cathodic sites.

All these explanations confirm that **1** is a good candidate against corrosion thanks to the panoply of atoms in its structure, namely a copper transition metal characterized solely by a high corrosion resistance, nitrogen and oxygen which are qualified by an electronegativity able to establish bonds with the active sites of the metal. Therefore, one can ascribe this inhibiting efficiency which reaches 92% to a synergic effect between all the atoms of the structure of **1.**

Table 8

EIS parameters and inhibition efficiency for MS in 1 M HCl at different concentrations of complex **1**.

Mild steel/ 1M HCl + {C_i mol L^{-1} of **1**}	0	1×10^{-6}	1×10^{-5}	1×10^{-4}	1×10^{-3}
Rs {Ω cm^2}	0.782 ± 0.004	0.837 ± 0.004	0.836 ± 0.004	0.818 ± 0.004	0.753 ± 0.004
10^6 Q_{dl} {s^n Ω^{-1} cm^{-2}}	276.05 ± 3.14	201.67 ± 8.58	195.46 ± 5.79	149.48 ± 3.99	113.17 ± 2.49
n_{CPE1}=n_{dl}	0.826 ± 0.001	0.868 ± 0.004	0.863 ± 0.003	0.870 ± 0.003	0.876 ± 0.002
R_{ct} {Ω cm^2}	-	33.15 ± 3.04	50.37 ± 2.94	64.06 ± 3.48	81.85 ± 3.24
10^6 Q_f {s^n Ω^{-1} cm^{-2}}	-	805 ± 37	590 ± 18	386 ± 12	262 ± 6.00
n_{CPE2}=n_f	-	0.638 ± 0.014	0.694 ± 0.012	0.720 ± 0.012	0.754 ± 0.008
R_f {Ω cm^2}	-	74.24 ± 3.31	128.70 ± 3.40	155.60 ± 3.95	395.20 ± 4.627
R_p {Ω cm^2}	33.86 ± 0.07	107.39 ± 3.18	179.07 ± 3.17	219.66 ± 3.71	477.05 ± 3.43
10^4 χ^2	6.63	3.37	3.09	2.96	3.02
η_{EIS}		68%	81%	84%	92%

3.7.3. Adsorption isotherms

Adsorption of an inhibitor to a metal surface, in general, can be held either by electrostatic attraction of charged metal and charged inhibitor, non-shared electron pairs in the inhibitor interact with the metal through a dipole interaction, π-interaction with the metal, or by the combination of all the above [88]. Because the adsorption phenomenon takes place at the interface essentially throughout charge transfer and a coordinating bound is formed between inhibitor and metal; the process here is termed chemisorption, but it cannot be denied that there could be a physical type of adsorption. In corrosion inhibition, the adsorption is assumed to be due to the substitution of x number of water molecules adsorbed at a surface by an inhibitor molecule in the aqueous phase (Equation (11)).

$$inh_{(aq)} + xH_2O_{(sur)} = inh_{(sur)} + xH_2O_{(aq)} \qquad (11)$$

This consideration that the corrosion inhibition governed by equation (11) seems to be an oversimplification [89]. In actuality, the adsorption phenomena depend on a number of variables, including surface state, the inhibitor's electrical properties, multilayer adsorption, and different levels of surface-site activity. This involved presenting various isotherm models to study the links between corrosion rate and inhibitor concentration. Essentially, all isotherms that are known have the form of Equation (12):

$$f(\theta,x)\ \exp(-a\theta) = KC_{inh} \qquad (12)$$

where θ is the surface coverage, x is the size ratio, or the relative size of the solute and solvent molecules, a measure the molecular interaction between the adsorption layer and the degree of surface heterogeneity, K is the constant adsorption equilibrium, and C_{inh} is the inhibitor concentration. It's interesting to note that none of the accessible isotherms expressly contain both 'x' and 'a' and none of them have an expression that does. The adsorption isotherms used to fit the experimental data, are Frumkin and Temkin depending on lateral interaction parameter ‘a’ describing the molecular interactions in the adsorption layer and the heterogeneity of the surface. On the other hand, the kinetic-thermodynamic model of El-Awady and Flory-Huggins, based on the relative size of the inhibitor molecule to the solvent molecule adsorbed to the surface or active site. The conventional and linearized forms of isotherms are presented in Table 9.

Table 9

Conventional and linearized forms of isotherms used.

Isotherm	**Conventional form**	**Linearized form**	
El-Awady	$\left(\frac{\theta}{1-\theta}\right)^{1/y} = K_{ads}C_{inh}$	$\log\left(\frac{\theta}{1-\theta}\right) = y\log K_{ads} + y\log C_{inh}$	[89]
Temkin	$\exp(-2a\theta) = K_{ads}C_{inh}$	$\theta = -\frac{1}{2a}\ln K_{ads} - \frac{1}{2a}\ln C_{inh}$	[90]
Frumkin	$\frac{\theta}{1-\theta}e^{-2a\theta} = K_{ads}C_{inh}$	$\ln\frac{\theta}{\left(C_{inh}(1-\theta)\right)} = \ln K_{ads} + 2a\theta$	[91]
Flory-Huggins	$\frac{\theta}{x(1-\theta)^{x}} = K_{ads}C_{inh}$	$\log\left(\frac{\theta}{C_{inh}}\right) = \log(xK_{ads}) + x\log(1-\theta)$	[92]

The adsorption of the inhibitor on the metal occurs because the interaction energy between the metal and the inhibitor is more favorable than the interaction energy between the metal and electroactive molecules responsible for the corrosion of the metal molecules. The free energy is related to the temperature by Equation (13):

$$\Delta_r G^{\circ}_{ads} = -RT\ln(55.5K_{ads}) \qquad (13)$$

where T and R are the thermodynamic temperature and the gas constant, respectively. 55.5 is the mole concentration of water (mol L^{-1}).

The ratio $\eta_{EIS}\%/100 = \theta$ is used in the current investigation to calculate values of θ [93], which correspond to various concentrations of **1**. Figure 18 exemplifies the curves related to Temkin, El-Awady, Frumkin and Flory-Huggins adsorption isotherm models. Table 10 compiles the adsorption parameters that can be inferred from these isotherms.

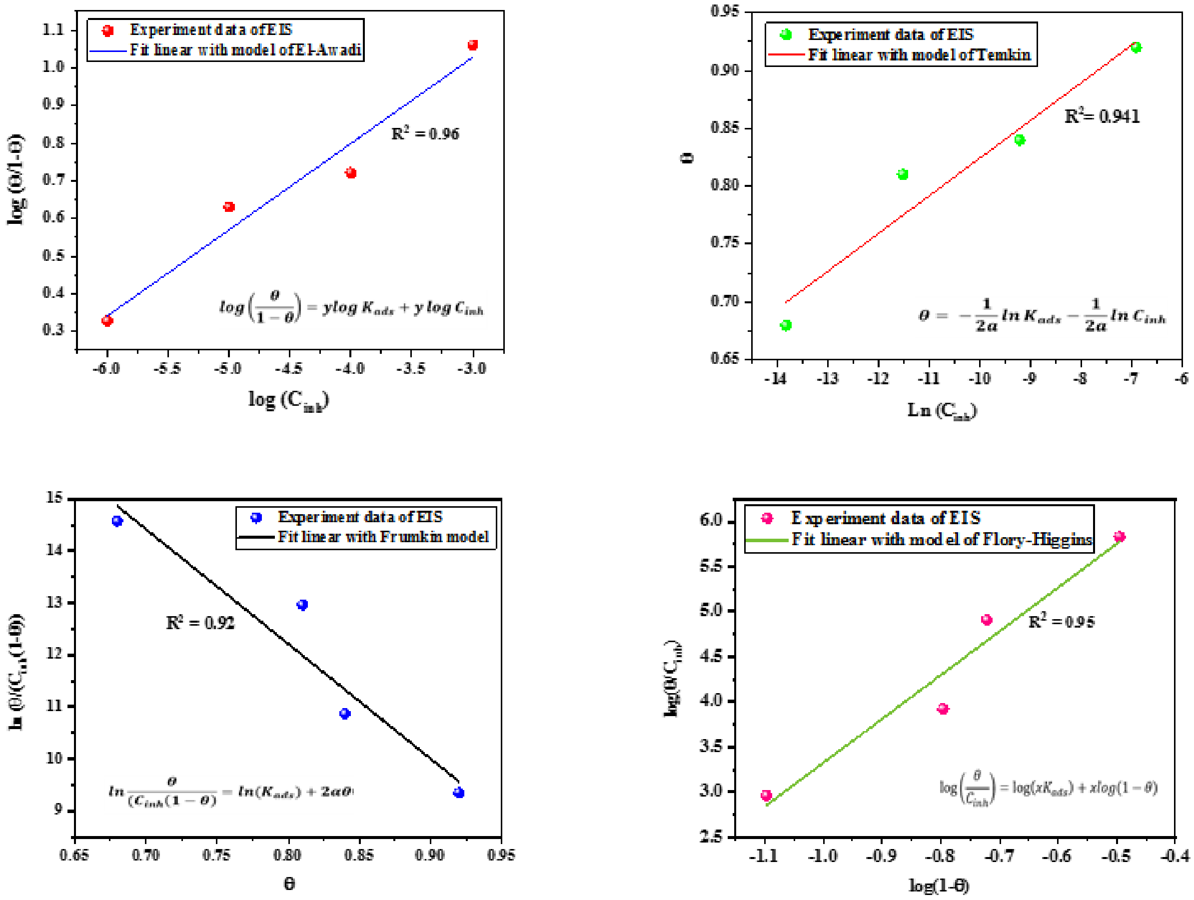

Figure 18: Plots of the adsorption isotherm models of $(C_4H_{16}N_3)[Cu(NO_3)(C_2O_4)_2].2H_2O$ for MS surface in 1 M HCl at 298 K obtained from EIS data.

Table 10 shows that all the determination coefficients are higher than 0.9, suggesting that the results could obey the proposed isotherm models. The reciprocal of ‘y’ obtained from El-Awady isotherm is nearly equal to 4.54 implying that four activated sites have been fulfilled by one molecule of $(H_3dien)[Cu(NO_3)(C_2O_4)_2].2H_2O$ in the inhibition process, through the variety of anions and cations in the structure of the complex **1**. However, ‘x’ parameter derived from Flory-Huggins model is equal to 4.85, meaning that approximately four molecules of solvent which is already adsorbed on the surface are substituted by one molecule of $(C_4H_{16}N_3)[Cu(NO_3)(C_2O_4)_2].2H_2O$. This exhibits a good agreement with the El-Awady model, and it can be concluded that four active sites occupied initially by solvent molecules (H^+, Cl^- or H_2O) have been substituted with one molecule of complex **1**. This agreement is observed even in the values of K_{ads} and $\Delta_rG°(ads)$ which assumed that the adsorption of $(H_3dien)[Cu(NO_3)(C_2O_4)_2].2H_2O$ at MS surface is a spontaneous process [94]. According to Frumkin and Temkin's calculations, the value of the lateral interactive parameter "a" was found to be high and negative, which is interpreted to mean that there is a strong interaction between the inhibitor molecules adsorbed to the surface, making the developed layer more persistent and conferring a good efficiency inhibitor. Also, the negative values of $\Delta_rG°(ads)$ demonstrate that the adsorption of $(C_4H_{16}N_3)[Cu(NO_3)(C_2O_4)_2].2H_2O$ onto the MS surface is highly favored in acidic medium. All the findings demonstrate the widespread application of the Langmuir isotherm, which states that the metal surface is homogeneous, contains a fixed number of adsorption sites and each site can only hold one adsorbate inhibitor molecule. This is not the case in this study; instead, the heterogeneous nature of the MS surface is supported by the average value of the exponent CPE_{dl}, which is 0.9 [76, 95].

Table 10

Adsorption parameters deducted from linearizing various adsorption isotherms for MS in 1M HCl in the presence of complex **1** at 298 K.

Isotherm	K_{ads} (L.mol^{-1})	$\Delta_rG°$ (Kj.mol^{-1})	Isotherm property
El-Awady	30.84×10^6	-52.67×10^3	1/y = 4.54
Temkin	4×10^{15}	-98.95×10^3	a = -15.62
Frumkin	9.20×10^{12}	-83.90×10^3	a = -11.02
Flory-Huggins	31.20×10^6	-52.70×10^3	x = 4.85

Conclusion

We synthesized $(C_4H_{16}N_3)[Cu(NO_3)(C_2O_4)_2].2H_2O$ utilizing a wet chemistry method. It was characterized by single crystal X-ray diffraction, Fourier Transform Infrared spectroscopy (FTIR) and assessed for thermal stability (TG-DTA). FT-IR measurements were used to validate the presence of the different bands made up of the diethylenetriammonium cation, nitrate, and oxalate. The crystal structure of **1** is described as a 3D framework in which

$[Cu_2(C_2O_4)_4(NO_3)_2]$ dimers interact via the H-Bonds network and weak electrostatic interactions. Compound **1** is stable up to 140°C, according to research employing thermogravimetry. The Curie-Weiss temperature is lower than 2 K, **1** shows paramagnetic behaviour for temperatures above 1 K. Its catalytic investigation showed that the title compound is a very promising choice for nitro function reduction. All of the nitrophenol isomers, 2-NP, 3-NP, and 4-NP, were reduced to aminophenol isomers, and this process was particularly successful for the complex under investigation. These characteristics make compound **1** applicable as a catalyst in the conversion of nitro groups to amine functionalities. Furthermore, it exhibits a high anticorrosive activity for mild steel in acidic medium. The polarization resistances obtained by LPR are in agreement with the values obtained by EIS thanks to the non-destructive character of the two methods. The process of corrosion inhibition in the presence of **1** takes place at the mild steel interface by two stages. The isotherms used to fit the data for understanding the adsorption phenomena show a good agreement with the model based on lateral interaction and size ratio/or active sites parameters. The values of free energy $\Delta_r G°(ads)$ indicate that the process of adsorption involves by chemisorption.

Author Contributions

All authors have given approval to the final version of the manuscript. CRediT: Mohamed Akouibaa conducted the synthesis and the physicochemical characterization of the material under study, writing-original draft; Mariya Kadiri and Majid Driouch: carried out the anti-corrosion study; Karim Tanji carried out the photocatalytic study; Rachid Ouarsal carried out the infrared and thermal study; Souâd Rakib resources, methodology, writing-review & editing; Mouhcine Sfaira resources, writing the anti-corrosion part; Nicola Morley carried out the magnetic study and writing this part; Mohammed Lachkar project administration, supervision, conceptualization, funding acquisition, methodology, resources, writing-review & editing;

Brahim El Bali: project administration, methodology, writing-review & editing; Abdelkader Zarrouk investigation, writing-review & editing; El-Eulmi Bendeif solved and refined the X-ray structure, writing-review & editing.

Acknowledgements

We are grateful for measurement time on the X-ray diffraction platform PMD²X of the CPM Scientific pole, Université de Lorraine, France.

References

[1] K.I. Abdallah, S. Mohamed, R. Mohamed and G. Abdelhalim, Bis(ammonium) tris (hexaaquamagnesium) tetrakis(hydrogen phosphite), Acta Crystallogr., Sect. C: Cryst. Struct. Commun. 62 (2006) i43-i45. https://doi.org/10.1107/S0108270106008882.

[2] T.D. Keene, H.R. Ogilvie, M.B. Hursthouse, D.J. Price, One-dimensional magnetism in new, layered structures: piperazine-linked copper and nickel oxalate chains, Eur. J. Inorg. Chem. 2004 (2004) 1007-1013. https://doi.org/10.1002/ejic.200300592.

[3] A. Timothy Royappa, A.D. Royappa, R.F. Moral, A.L. Rheingold, R.J. Papoular, D.M. Blum, T.Q. Duong, J.R. Stepherson, O.D. Vu, B. Chen, M.R. Suchomel, J.A. Golen, G. André, N. Kourkoumelis, A.D. Mercer, A.M. Pekarek, D.C. Kellya, Copper (I) oxalate complexes: synthesis, structures and surprises, Polyhedron. 119 (2016) 563-574. https://doi.org/10.1016/j.poly.2016.09.043.

[4] B. Zhang, Y. Zhang, Z. Wang, S. Gao, Y. Guo, F. Liue and D. Zhua, $BETS_3[Cu_2(C_2O_4)_3](CH_3OH)_2$: an organic-inorganic hybrid antiferromagnetic metal (BETS = bisethylene (tetraselenfulvalene)), Cryst. Eng. Comm. 15 (2013) 3529-3535. https://doi.org/10.1039/C2CE26552D.

[5] M. Akouibaa, N. Hamdi, H. Hassani, Oudghiri. S. Rakib, M. Lachkar, I. da Silva, B. El Bali, $[Ni(N_2H_5)_2(C_2O_4)_2].2H_2O$: Formation, crystal structure, catalytic performance and

sorbence activities, Physica B: Condensed Matter. 635 (2022) 413857. https://doi.org/10.1016/j.physb.2022.413857.

[6] G. Alzuet, S. Ferrer-Llusar, J. Borrás, R. Martínez-Mánez, New Cu(II) and Zn(II) complexes of benzolamide with diethylenetriamine: synthesis, spectroscopy and X-ray structures, Polyhedron. 19 (2000) 725-730. https://doi.org/10.1016/S0277-5387(00)00319-3

[7] R. Vaidhyanathan, S. Natarajan, et C.N.R. Rao, Synthesis of a hierarchy of zinc oxalate structures from amine oxalates, J. Chem. Soc., Dalton Trans. 5 (2001) 699-706. https://doi.org/10.1039/B008571P.

[8] R. Vaidhyanathan, S. Natarajan, A.K. Cheetham, C.N.R. Rao, New open-framework zinc oxalates synthesized in the presence of structure-directing organic amines, Chem. Mater. 11 (1999) 3636-3642. https://doi.org/10.1021/cm990434x.

[9] O.R. Evans, et W. Lin, Synthesis of zinc oxalate coordination polymers via unprecedented oxidative coupling of methanol to oxalic acid, Cryst. Growth Des. 1 (2001) 9-11. https://doi.org/10.1021/cg005508s.

[10] S. Natarajan, Synthesis and structure of a zinc oxalate with honeycomb layers and zinc phosphates with one-and three-dimensional structures, Solid State Sci. 4 (2002) 1331-1342. https://doi.org/10.1016/S1293-2558(02)00005-5.

[11] R. Vaidhyanathan, S. Natarajan, et C.N.R. Rao, Hybrid inorganic-organic host-guest compounds: Open-framework cadmium oxalates incorporating novel extended structures of alkali halides, Chem. Mater. 13 (2001) 3524-3533. https://doi.org/10.1021/cm011011+.

[12] R. Vaidhyanathan, S. Natarajan, et C.N.R. Rao, Open-framework cadmium oxalates with channels stabilized by alkali metal ions, J. Solid State Chem. 162 (2001) 150-157. https://doi.org/10.1006/jssc.2001.9186.

[13] A.N. Puzan, V.N. Baumer, V.V. Vashchenko, D.S. Sofronov, Polymorphism of anhydrous cadmium oxalate CdC_2O_4, J. Alloys Compd. 726 (2017) 751-757. https://doi.org/10.1016/j.jallcom.2017.08.047.

[14] E. Jeanneau, N. Audebrand, J.-P. Auffrédica and D. Louër, Crystal structure, thermal behaviour and zeolitic properties of $Cd_2Zr\ (C_2O_4)_4{\cdot}(4+n)H_2O$, J. Mater. Chem. 11 (2001) 2545-2552. https://doi.org/10.1039/B103711K.

[15] R. Demichelis, Anhydrous cadmium oxalate polymorphism: a first principal study, Cryst. Eng. Comm. 21 (2019) 7123-7129. https://doi.org/10.1039/C9CE01232J.

[16] E. Jeanneau, N. Audebrand, et D. Louër, Synthesis, crystal structure and thermal behaviour of $CdZrK_2(C_2O_4)_4{\cdot}8H_2O$, J. Mater. Chem. 12 (2002) 2383-2389. https://doi.org/10.1039/B202463M.

[17] E. Jeanneau, N. Audebrand, et D. Louër, New open-framework ammonium and amine cadmium zirconium oxalates with helical structures, Chem. Mater. 14 (2002) 1187-1194. https://doi.org/10.1021/cm0112136.

[18] Z. Chen, Y. Zhou, L. Weng, H. Zhang, D. Zhao, Hydrothermal synthesis of two layered indium oxalates with 12-membered apertures, J. Solid State Chem. 173 (2003) 435-441. https://doi.org/10.1016/S0022-4596(03)00139-7.

[19] R. Vaidhyanathan, S. Natarajan, et C.N.R. Rao, Three-dimensional open-framework neodymium oxalates with organic functional groups protruding in 12-member channels, Inorg. Chem. 41 (2002) 4496-4501. https://doi.org/10.1021/ic020197r.

[20] S. Gatfaoui, N. Issaoui, A. Mezni, F. Bardak, T. Roisnel, A. Atac, H. Marouani, Synthesis, structural and spectroscopic features, and investigation of bioactive nature of a novel organic-inorganic hybrid material 1H-1,2,4-triazole-4-ium trioxonitrate, J. Mol. Struct. 1150 (2017) 242-257. https://doi.org/10.1016/j.molstruc.2017.08.092.

[21] M.E. Davis, Ordered porous materials for emerging applications, Nature. 417 (2002) 813-821. https://doi.org/10.1038/nature00785.

[22] A. Corma, M.J. Díaz-Cabanas, J.L. Jorda, C. Martínez, M. Moliner, High-throughput synthesis and catalytic properties of a molecular sieve with 18-and 10-member rings, Nature. 443 (2006) 842-845. https://doi.org/10.1038/nature05238.

[23] B. Zhang, Y. Zhang, Z. Wang, D. Wang, D. Yang, Z. Gao, G. Chang, Y. Guo, T. Mori, Z. Zhao, F. Liu, Q. Li, D. Zhu, Organic-inorganic hybrid metallic conductors based on bis(ethylenedithio)tetrathiafulvalene cations and antiferromagnetic oxalate-bridged copper(II) dinuclear anions, J. Mater. Chem. C. 10 (2022) 2845-2852. https://doi.org/10.1039/D1TC04305F.

[24] C. Mee, C. Minchul, L. B.Soo. Chee-Hun, Structure, Magnetic and Ion-Exchange Properties of Self-Assembled Triaza-Copper(II)-Oxalate Hybrides Having Nanoscale One-Dimensional Channel, J. Nanosci. Nanotechnol. 6 (2006) 3338-3342. https://doi.org/10.1166/jnn.2006.005.

[25] S. Kawata, S. Kitagawa, M. Kondo, F. Isamu, M. Megumu, Two dimensional sheets of tetragonal copper (II) lattices: X-ray crystal structure and magnetic properties of $[Cu(C_6O_4Cl_2)(C_4H_4N_2)]_n$, Angew. Chem. Int. Ed. Engl. 33 (1994) 1759-1761, https://doi.org/10.1002/anie.199417591.

[26] S. Dehnen, M. Melullis, A coordination chemistry approach towards ternary M/14/16 anions, Coord. Chem. Rev. 251 (2007) 1259-1280, https://doi.org/10.1016/j. ccr.2006.11.003.

[27] P. Feng, X. Bu, N. Zheng, The interface chemistry between chalcogenide clusters and open framework chalcogenides, Acc. Chem. Res. 38 (2005) 293-303. https:// doi.org/10.1021/ar0401754.

[28] J. Yu, R. Xu, Chiral zeolitic materials: structural insights and synthetic challenges, J. Mater. Chem. 18 (2008) 4021-4030, https://doi.org/10.1039/B804136A.

[29] M.A. Deyab, B. El Bali, R. Essehli, R. Ouarsal, M. Lachkar, H. Fuess, $NaNi(H_2PO_3)_3 \cdot H_2O$ as a novel corrosion inhibitor for X70-steel in saline produced water, J. Mol. Liq. 216 (2016) 636-640. https://doi.org/10.1016/j.molliq.2016.01.075.

[30] M. Idboumlik, M. Kadiri, N. Hamdi, M. Driouch, A. F. I. Ngopoh, I. Lakkab, E. Bendeif, M. Sfaira, B. El Bali, M. Lachkar, A. Zarrouk, Synthesis of novel hybrid decavanadate material $(NH_4)_2(H_2en)_2\{V_{10}O_{28}\}.4H_2O$: Characterization, anticorrosion and biological activities, Mater. Chem. Phys. (2022) 126211. https://doi.org/10.1016/j.matchemphys.2022.126211.

[31] M.A. Deyab, R. Essehli B. El Bali, Inhibition of copper corrosion in cooling seawater under flowing conditions by novel pyrophosphate, RSC Adv. 5 (2015) 64326-64334. https://doi.org/10.1039/C5RA08119J.

[32] Z.A. Savel'eva, S.V. Larionov, G.V. Romanenko, N.V. Podberezskaya, & L.A. Sheludyakova, Zh. Neorg. Khim, Preparation and crystal and molecular structure of ethylenediammonium and diethylenetriammonium bis(oxalato)cuprate(II), (Russ. J. Inorg. Chem.) 37 (1992) 1094-1102. (In Russian).

[33] Rigaku Oxford Diffraction. CrysAlis CCD and CrysAlis RED. (*Versions 1.171.39.46*)], (2018).

[34] G.M. Sheldrick, SHELXT-Integrated space-group and crystal-structure determination. Acta Crystallogr. A. C71 (2015) 3-8. https://doi.org/10.1107/S2053273314026370.

[35] L.J. Farrugia, WinGX suite for small-molecule single-crystal crystallography, J. Appl. Crystallogr. 32 (1999) 837-838. https://doi.org/10.1107/S0021889899006020.

[36] K. Brandenburg K, H. Putz. Crystal Impact GbR, Postfach 1251, D 53002 Bonn, (2005) Germany.

[37] M.E. Fleet, Distortion parameters for coordination polyhedral, Mineral. Mag. 40 (1976) 531-533. https://doi.org/10.1180/minmag.1976.040.313.18.

[38] K. Robinson, G.V. Gibbs, P.H. Ribbe, Quadratic elongation: a quantitative measure of distortion in coordination polyhedral, Science. 172 (3983) (1971) 567-570. https://10.1126/science.172.3983.567.

[39] M. Akouibaa, H.O. Hassani, R. Ouarsal, S. Rakib, M. Lachkar, M. Poupon, M. Dusek, N. Morley and B. El Bali, $(H_3dien)[Ni(NO_3)(C_2O_4)_2].2H_2O$: Synthesis, crystal structure, catalytic activity and magnetic study, Chem. Data Collect. 42 (2022) 100969.

[40] P. Roman, C. Guzman-Miralles, A. Luque, I. B. Javier, C. Juan, L. Francesc, J. Miguel and A. Santiago, Influence of the peripheral ligand atoms on the exchange interaction in oxalato-bridged nickel (II) complexes: an orbital model. Crystal structures and magnetic properties of $(H_3dien)_2[Ni_2(ox)_5].12H_2O$ and $[Ni_2(dien)_2(H_2O)_2(ox)]Cl_2$, Inorg. Chem. 135 (996) 3741-3751. https://doi.org/10.1021/ic951081g.

[41] P. Sun, S. Liu, D. Feng, F. Ma, W. Zhang, Y. Ren, J. Cao, A novel organic-inorganic hybrid based on a dinuclear copper(II) oxalate complex, a α-metatungstate cluster $[H_2W_{12}O_{40}]^{6-}$ with catalytic activity in H_2O_2 decomposition, J. Mol. Struct. 968 (2010) 89-92. https://doi.org/10.1016/j.molstruc.2010.01.028.

[42] F. Guo, et W. Yu, Crystal structure of 1,10-phenanthrolinecopper(II) dinitrate, $[Cu(C_{12}H_8N_2)](NO_3)_2$, Z. fur Krist. - New Cryst. Struct. 223 (2008) 399-400. https://doi.org/10.1524/ncrs.2008.223.4.399.

[43] F.M. Shen and S.F. Lush, Crystal structure of (nitrato-κO)bis(1,10-phenanthroline-κ^2N,N')copper(II) nitrate gallic acid monosolvate monohydrate, Acta Cryst. E72 (2016) 1577-1580. https://doi.org/10.1107/S2056989016016066.

[44] B. Zina. D. Amani. S. Koray. B. El Bali. M. Lachkar. N. Benali-Cherif, Crystal structure, Hirshfeld surface analysis and theoretical calculations of an oxalato-bridged copper (II) complex: μ-oxalato-bis[(2,2'-bipyridine) hydrate copper(II) nitrate], J. Iran. Chem. Soc. 17 (2020) 671-685. https://doi.org/10.1007/s13738-019-01805-0.

[45] T.D. Keene, M.B. Hursthouse, D.J. Price, Stabilization of discrete $[Cu(C_2O_4)_2(H_2O)_2]^{2-}$ dianions in the solid state by an extensive hydrogen bonded network, Z. Anorg. Allg. Chem. 630 (2004) 350-352. https://doi.org/doi.org/10.1002/zaac.200300373.

[46] N. Audebrand, S. Raite, D. Louër, The layer crystal structure of $[In_2(C_2O_4)_3(H_2O)_3]\cdot 7H_2O$ and microstructure of nanocrystalline In_2O_3 obtained from thermal decomposition, Solid State Sci. 5 (2003) 783-794. https://doi.org/10.1016/S1293-2558(03)00084-0.

[47] F. Öztürk, İ. Bulut, Y. Bekiroğlu, A. Bulut, Spectroscopic, structural, electrochemical and anti-microbiological studies of Cu(II)-sulfathiazole complex with diethylenetriamine ligand, Polyhedron. 119 (2016) 420-428. https://doi.org/10.1016/j.poly.2016.07.019.

[48] N. Rekik, N. Issaoui, H. Ghalla, B. Oujia, M.J. Wójcik, IR spectral density of H-bonds. Both intrinsic anharmonicity of the fast mode and the H-bond bridge. Part I: Anharmonic coupling parameter and temperature effects, J. Mol. Struct. Theochem. 821 (2007) 9-21. https://doi.org/10.1016/j.theochem.2007.06.016.

[49] W. Yao, S.H. Yu, J. Jiang, L. Zhang, Complex wurtzite ZnSe microspheres with high hierarchy and their optical properties, Chem. Eur. J. 12 (2006) 2066-2072. https://doi.org/10.1002/chem.200500835.

[50] X. Chen, et X. Cai, Synthesis of poly (diethylenetriamine terephthalamide) and its application as a flame retardant for ABS, J. Therm. Anal. Calorim. 125 (2016) 313-320. https://doi.org/10.1007/s10973-016-5358-1

[51] N. Issaoui, H. Ghalla, F. Bardak, M. Karabacak, N. Aouled Dlal, H.T. Flakus, B. Oujia, Combined experimental and theoretical studies on the molecular structures, spectroscopy, and inhibitor activity of 3-(2-thienyl) acrylic acid through AIM, NBO, FT-IR, FT-Raman, UV and HOMO-LUMO analyses, and molecular docking, J. Mol. Struct. 1130 (2017) 659-668. https://doi.org/10.1016/j.molstruc.2016.11.019.

[52] A.S. Kazachenko, F. Akman, A. Sagaama, N. Issaoui, Y.N. Malyar, N.Y. Vasilieva, V.S. Borovkova, Theoretical and experimental study of guar gum sulfation, J. Mol. Model. 27 (2021) 1-15. https://doi.org/10.1007/s00894-020-04645-5.

[53] Y.G. Denisenko, M.S. Molokeev, A.S. Oreshonkov, A.S. Krylov, A.S. Aleksandrovsky, N.O. Azarapin, O.V. Andreev, I.A. Razumkova, V.V. Atuchin, Crystal Structure, Vibrational, Spectroscopic and Thermochemical Properties of Double Sulfate Crystalline Hydrate $[CsEu(H_2O)_3(SO_4)_2]\cdot H_2O$ and Its Thermal Dehydration Product $CsEu(SO_4)_2$, Crystals. 11 (2021) 1027. https://doi.org/10.3390/cryst11091027.

[54] N.N. Golovnev, M.S. Molokeev, I.V. Sterkhova, M.K. Lesnikov, V.V. Atuchin, Coordination effects in hydrated manganese (II) 1,3-diethyl-2-thiobarbiturates and their thermal stability, Polyhedron. 134 (2017) 120-125. https://doi.org/10.1016/j.poly.2017.06.002.

[55] M.L. Feng, H.Y. Ye, J.G. Mao, Syntheses, crystal structures and photoluminescence properties of three novel organically bonded indium selenates or selenites, J. Solid State Chem. 180 (2007) 2471- 2477. https://doi.org/10.1016/j.jssc.2007.06.022.

[56] M. Trpkovska, B. Šoptrajanov, L. Pejov, Reinvestigation of the infrared spectra of calcium oxalate monohydrate and its partially deuterated analogues, Bull. Chem. Technol., Macedonia. 21 (2002) 111-116.

[57] N. Issaoui, N. Rekik, B. Oujia, M.J. Wójcik, Theoretical infrared line shapes of H-bonds within the strong anharmonic coupling theory and Fermi resonances effects, Int. J. Quantum Chem. 110 (2010) 2583-2602. https://doi.org/10.1002/qua.22395.

[58] D.J. Goebbert, E. Garand, T. Wende, R. Bergmann, G. Meijer, K.R. Asmis, D.M. Neumark, Infrared spectroscopy of the microhydrated nitrate ions $(NO_3)^{-}(H_2O)_{1-6}$, J. Phys. Chem., A. 113 (2009) 7584-7592. https://doi.org/10.1021/jp9017103.

[59] N. Zotov, K. Petrov, et Dimitrova-Pankova, M, Infrared spectra of Cu(II)-Co(II) mixed hydroxide nitrates, J. Phys. Chem. Solids. 51 (1990) 1199-1205.

https://doi.org/10.1016/0022-3697(90)90102-L.

[60] N. Logan, et W.B. Simpson, The infra-red spectra of copper (II) nitrate and it adducts with some organic oxygen and nitrogen donor molecules, Spectrochimica Acta. 21 (1965) 857-860. https://doi.org/10.1016/0371-1951(65)80152-7.

[61] N.F. Curtis, et Y.M. Curtis, Some nitrato-amine nickel (II) compounds with monodentate and bidentate nitrate ions, Inorg. Chem. 4 (1965) 804-809. https://doi.org/10.1021/ic50028a007.

[62] B.M. Gatehouse, et A.E. Comyns, Infrared spectra of uranyl nitrate hydrates and rubidium uranyl nitrate, J. Chem. Soc. (Resumed) (1958) 3965-3971. https://doi.org/10.1039/JR9580003965.

[63] M. Akouibaa, I. Lakkab, A. Direm, M. Lachkar, R. Ouarsal, S. Rakib, V. Nasif, K. Sayin, N. Morley, B. El Bali, $[Cu_2(ox)(dien)_2](NO_3)_3$, a precursor for preparation of CuO nanoparticles: synthesis, structural, Hirshfeld surface analyses, and physico-chemical investigations, J. Mol. Struct. 1282 (2023) 135258. https://doi.org/10.1016/j.molstruc.2023.135258.

[64] N. Rekik, N. Issaoui, B. Oujia, M.J. Wójcik, Theoretical IR spectral density of H-bond in liquid phase: Combined effects of anharmonicities, Fermi resonances, direct and indirect relaxations, J. Mol. Liq. 141 (2008) 104-109. https://doi.org/10.1016/j.molliq.2007.10.009.

[65] K. Nakamoto, Coordination Compounds. In Infrared and Raman Spectra of Inorganic and Coordination Compounds, part B application in coordination organometallic and bioinorganic chemistry 4th Ed., Wiley: New York 1986.

[66] J. Buse, V. Otero and M.J. Melo, New insights into synthetic copper greens: the search for specific signatures by Raman and infrared spectroscopy for their characterization in medieval artworks, Heritage. 2 (2019) 1614-1629. https://doi.org/10.3390/heritage2020099.

[67] H.G.M. Edwards, D.W. Farwell, S.J. Rose, D.N. Smith, Vibrational spectra of copper (II) oxalate dihydrate, $CuC_2O_4·2H_2O$, and dipotassium bis-oxalato copper (II) tetrahydrate, $K_2Cu(C_2O_4)_2·4H_2O$, J. Mol. Struct. 249 (1991) 233-243. https://doi.org/10.1016/0022-2860(91)85070-J.

[68] S. Hidaoui, N. Hamdi, M. Akouibaa, R. Benali-Cherif, E. Vaclav, M. Dusek, M. Lachkar, B. El Bali, Synthesis, Crystal structure and catalytic activity of the new hybrid phosphate $(C_4H_{12}N_2)[Co(H_2O)_6](HPO_4)_2$, J. Mol. Struct. 1265 (2022) 133296. https://doi.org/10.1016/j.molstruc.2022.133296.

[69] H.O Hassani, M. Akouibaa, S. Rakass, M. Abboudi, B. El Bali, M. Lachkar, F. Al Wadaani, A simple and cost-effective new synthesis method of copper molybdate $CuMoO_4$ nanoparticles and their catalytic performance, J. Sci. Adv. Mater. Devices. 6 (2021) 501-507, https://doi.org/10.1016/j.jsamd.2021.06.003.

[70] O. Długosz, K. Szostak, M. Krupiński, M. Banach, Synthesis of Fe_3O_4/ZnO nanoparticles and their application for the photodegradation of anionic and cationic dyes, Int. J. Environ. Sci. Technol. 18 (2021) 561-574. https://doi.org/10.1007/s13762-020-02852-4.

[71] G. Augusto, R.D. Oliveira, D.M. Leme, J. de Lapuente, L.B. Brito, C. Porredón, L. de Brito Rodrigues, N. Brull, J.T. Serret, M. Borràs, G. Rodrigo Disner, M.M. Cestari, D. Palma de Oliveira, Chemico-Biological Interactions A test battery for assessing the ecotoxic effects of textile dyes, Chem. Biol. Interact. 291 (2018) 171-179. https://doi.org/10.1016/j.cbi.2018.06.026.

[72] P. Mahawar, A. Akhtar, Impact of dye effluent on seed germination, seedling growth and chlorophyll content of soybean (Glycine max L.), Int. J. Sci. Res. 8 (2019) 1-5. https://doi.org/10.21275/ART20201601.

[73] C. Wagner, W. Traud, The interpretation of corrosion phenomena by super-imposition of electrochemical partial reactions and the formation of potentials of mixed electrodes, Z. Elektrochem. 44 (1938) 391-402.

[74] K.F. Bonhoeffer, W. Jena, Über das elektromotorische Verhalten von Eisen, Zeitschrift für Elektrochemie und Angewandte Physikalische Chemie. 55 (1951) 151-154. https://doi.org/10.1002/bbpc.19510550215.

[75] M. Stern, A.L. Geary, Electrochemical polarization: I. A theoretical analysis of the shape of polarization curves, J. Electrochem. Soc. 104 (1957) 56. https://doi.org/10.1149/1.2428496.

[76] S. Aourabi, M. Driouch, M. Sfaira, F. Mahjoubi, B. Hammouti, C. Verma, E.E. Ebenso, L. Guo, Phenolic fraction of Ammi visnaga extract as environmentally friendly antioxidant and corrosion inhibitor for mild steel in acidic medium, J. Mol. Liq. 323 (2021) 114950. https://doi.org/10.1016/j.molliq.2020.114950.

[77] A.N.S. Shamaya, O.H.R. Al-Jeilawi, N. Ali Khudhair, Novel Synthesis of Some N-Hydroxy Phthalimide Derivatives with Investigation of Its Corrosion Inhibition for Carbon Steel in HCl Solution, Chem. Methodol. 5 (2021) 331-340. https://doi.org/10.22034/chemm.2021.131305.

[78] F. Mansfeld, The polarization resistance technique for measuring corrosion currents, Corros. Sci. Technol. (1976) 163-262. https://doi.org/10.1007/978-1-4684-8986-6-3.

[79] H. Fricke. XXXIII. The theory of electrolytic polarization. Lond. Edinb. Dublin philos. Mag. J. Sci.,14 (1932) 310-318. https://doi.org/10.1080/14786443209462064.

[80] K.S. Cole, R.H. Cole, Dispersion and absorption in dielectrics. I. Alternating current characteristics, J. Chem. Phys. 9 (1941) 341-351. https://doi.org/10.1063/1.1750906.

[81] D.W. Davidson, R.H. Cole, Dielectric relaxation in glycerol, propylene glycol, and n-propanol, J. Chem. Phys. 19 (1951) 1484-1490. https://doi.org/10.1063/1.1748105.

[82] F. Mansfeld, H. Shih, H. Greene, C.H. Tsai, Analysis of EIS Data for Common Corrosion Processes, Electrochemical Impedance: Analysis and Interpretation. ASTM STP. 1188 (1993) 37-53. https://doi.org/10.1520/STP18062S.

[83] A. Popova, M. Christov, A. Vasilev, Inhibitive properties of quaternary ammonium bromides of N-containing heterocycles on acid mild steel corrosion. Part II: EIS results. Corr Sci. 49. (2007) 3290-3302. https://doi.org/10.1016/j.corsci.2007.03.012.

[84] A. Popova, S. Raicheva, E. Sokolova, M. Christov, Frequency dispersion of the interfacial impedance at mild steel Corrosion in acid media in the presence of benzimidazole derivatives, Langmuir. 12 (1996) 2083-2089. https://doi.org/10.1021/la950148+.

[85] A. Bonnel, F. Dabosi, C. Deslouis, M. Duprat, M. Keddam, B. Tribollet, Corrosion study of a carbon steel in neutral chloride solutions by impedance techniques, J. Electrochem. Soc. 130 (1983) 753-761. https://doi.org/10.1149/1.2119798.

[86] C. Vermaa, I.B. Obot, I. Bahadura, S.M. Sherif, Choline based ionic liquids as sustainable corrosion inhibitors on mild steel surface in acidic medium: Gravimetric, electrochemical, surface morphology, DFT and Monte Carlo simulation studies, J. Appl. Surf. Sci. 457 (2018) 134-149. https://doi.org/10.1016/j.apsusc.2018.06.035.

[87] K.S.M. Ferigita, M.G.K. AlFalah, M. Saracoglu, Z. Kokbudak, S. Kaya, M.O.A. Alaghani, F. Kandemirli, Corrosion behaviour of new oxo-pyrimidine derivatives on mild steel in acidic media: Experimental, surface characterization, theoretical, and Monte Carlo studies, J. Appl. Surf. Sci. Adv. 7 (2022) 100200. https://doi.org/10.1016/j.apsadv.2021.100200.

[88] T.O. Esan, O.E. Oyeneyin, A.D. Olanipekun, N. Ipinloju, Corrosion inhibitive potentials of some amino acid derivatives of 1,4-naphthoquinone-DFT calculations, Adv. J. Chem. A. 5 (2022) 263-270. https://doi.org/10.22034/AJCA.2022.353882.1321.

[89] A.A. El-Awady, B.A. Abd-El-Nabey, S.G. Aziz, Kinetic-thermodynamic and adsorption isotherms analyses for the inhibition of the acid corrosion of steel by cyclic and open-chain amines, J. Electrochem. Soc. 139 (1992) 2149. https://doi.org/10.1149/1.2221193.

[90] M. Temkin, V. Pyzhev, Kinetics of ammonia synthesis on promoted iron catalysts, Acta Physicochimica U.R.S.S. 12 (1940) 327-356.

[91] A.N. Frumkin, Z. Phys. Chem., 116 (1925) 166.

[92] B. Ateya, B. E1-Anadouli, and F. E1-Nizamy, The adsorption of thiourea on mild steel, Corros. Sci. 24 (1984) 509-515. https://doi.org/10.1016/0010-938X(84)90033-7.

[93] B. Maleki, A. Davoodi, M.V. Azghandi, M. Baghayeri, E. Akbarzadeh, H. Veisi, S.S. Ashrafi, M. Raei, Facile synthesis and investigation of 1,8-dioxooctahydroxanthene derivatives as corrosion inhibitors for mild steel in hydrochloric acid solution, New J. Chem. 40 (2016) 1278-1286. https://doi.org/10.1039/C5NJ02707A.

[94] N. Soltani, M. Khayatkashani, Evaluating performance of malva sylvestris leaf extract for protection of mild steel against corrosion in acidic solution, Asian J. Green. 5 (2021) 39-57. https://doi.org/10.22034/ajgc.2021.104987.

[95] A. Elmoussaoui, M. Kadiri, M. Bourhia, M. Chedadi, A. Agour, M. Sfaira, A. Bari, Promising antioxidant and anticorrosion activities of mild steel in 1.0 M hydrochloric acid solution by *Withania frutescens* L., essential oil, Front. Chem. 9 (2021) 739273. https://doi.org/10.3389/fchem.2021.739273.

Table 1

Crystal data, data collection and structure refinement of $(C_4H_{16}N_3)[Cu(NO_3)(C_2O_4)_2].2H_2O$.

Crystal data	
Chemical formula	$(C_4H_{16}N_3)[Cu(NO_3)(C_2O_4)_2].2H_2O$
M_r (g/mol)	887.66
Crystal system, space group	Monoclinic, $P2_1/c$
Temperature (K), Mo *K*α radiation, λ (Å)	100, 0.71073
a, b, c (Å)	10.1054 (5), 11.0825 (5), 14.8238 (7)
β	103.516 (5)
V ($Å^3$), Z	1614.18 (14), 2
F(000)	916
Crystal sizes (mm)	0.13 × 0.13 × 0.12
μ (mm^{-1})	1.43
D_x [Mg (m^{-3})]	1.826
R(int)	0.038
No. measured reflections	30899
No. independent reflections	6062
Reflections with $I > 2\sigma(I)$	5092
θ_{max} , θ_{min}	2.8–32.9°
T_{min} , T_{max}	0.829, 0.845
Reciprocal space	h = -15→15, k = -16→16, l = -22→22
$R[F2 > 2\sigma(F2)]$	0.026
wR(F2)	0.070

Table 2

Fractional atomic coordinates and isotropic or equivalent isotropic displacement parameters $(C_4H_{16}N_3)[Cu(NO_3)(C_2O_4)_2].2H_2O$.

	x	*y*	*z*	$U_{iso}*/U_{eq}$
Cu1	0.86594 (2)	0.59068 (2)	0.52739 (2)	0.00774 (4)
O1	0.85892 (9)	0.42600 (7)	0.48023 (6)	0.00949 (15)
O4	0.84879 (8)	0.67003 (7)	0.40828 (6)	0.00932 (15)
O2	0.88488 (8)	0.51556 (7)	0.64825 (6)	0.00930 (15)
O3	0.89734 (9)	0.75132 (7)	0.58048 (6)	0.00992 (15)
O6	0.83427 (9)	0.23907 (8)	0.53248 (6)	0.01188 (16)
O9	0.83677 (8)	0.85817 (7)	0.35194 (6)	0.00982 (15)
O7	0.89074 (9)	0.33068 (7)	0.70921 (6)	0.01069 (15)
O8	0.88131 (9)	0.94274 (8)	0.53023 (6)	0.01110 (16)
O5	0.61948 (9)	0.59629 (8)	0.49151 (7)	0.01329 (17)
O1W	0.44457 (10)	-0.09238 (9)	0.14686 (7)	0.01660 (18)
O2W	0.67818 (9)	0.76663 (8)	0.19242 (6)	0.01324 (16)
O10	0.59392 (10)	0.79166 (8)	0.49190 (7)	0.01613 (18)
O11	0.49299 (15)	0.68769 (11)	0.37293 (9)	0.0427 (4)
N2	0.43591 (10)	0.04055 (9)	0.29905 (7)	0.00934 (17)
N3	0.09116 (10)	-0.07797 (9)	0.30548 (7)	0.00863 (17)
N1	0.80908 (10)	0.11147 (9)	0.37250 (7)	0.00816 (16)
N4	0.56697 (11)	0.69249 (10)	0.45173 (7)	0.01343 (19)
C7	0.87833 (11)	0.83265 (10)	0.51740 (8)	0.00784 (18)
C5	0.85306 (11)	0.34881 (10)	0.54312 (7)	0.00775 (18)
C8	0.85224 (11)	0.78449 (10)	0.41661 (7)	0.00724 (18)
C6	0.87722 (11)	0.40021 (10)	0.64262 (8)	0.00745 (18)
C3	0.33465 (11)	-0.02779 (10)	0.33776 (8)	0.01011 (19)
C4	0.20046 (12)	-0.02662 (11)	0.26551 (8)	0.0107 (2)
C2	0.57259 (11)	0.04806 (11)	0.36411 (8)	0.01054 (19)
C1	0.66912 (12)	0.10805 (11)	0.31308 (8)	0.0105 (2)
H1W1	0.5233 (17)	-0.1315 (18)	0.1535 (14)	0.031 (5)*
H2W1	0.438 (3)	-0.043 (2)	0.0969 (14)	0.054 (7)*

H4A	0.1764 (17)	0.0523 (16)	0.2460 (12)	0.013 (4)*
H4B	0.2056 (19)	-0.0730 (16)	0.2137 (13)	0.020 (5)*
H3A	0.3262 (15)	0.0106 (14)	0.3927 (11)	0.006 (3)*
H1N2	0.4045 (16)	0.1166 (9)	0.2854 (12)	0.013 (4)*
H1A	0.6419 (17)	0.1917 (16)	0.2961 (12)	0.013 (4)*
H1N1	0.8631 (15)	0.1352 (16)	0.3357 (10)	0.018 (4)*
H2N1	0.8134 (17)	0.1626 (14)	0.4208 (9)	0.016 (4)*
H1B	0.6760 (17)	0.0637 (15)	0.2596 (12)	0.012 (4)*
H3N3	0.0103 (12)	-0.0694 (16)	0.2641 (10)	0.017 (4)*
H2N2	0.4427 (17)	0.0031 (14)	0.2450 (8)	0.015 (4)*
H3B	0.3655 (18)	-0.1084 (16)	0.3515 (12)	0.015 (4)*
H1W2	0.741 (2)	0.794 (2)	0.2426 (13)	0.040 (6)*
H2N3	0.1047 (18)	-0.1571 (9)	0.3166 (13)	0.022 (5)*
H1N3	0.0825 (18)	-0.0382 (15)	0.3568 (9)	0.020 (4)*
H2B	0.6037 (15)	-0.0323 (14)	0.3831 (11)	0.006 (3)*
H2A	0.5617 (17)	0.0953 (15)	0.4181 (12)	0.013 (4)*
H3N1	0.8309 (18)	0.0362 (10)	0.3929 (12)	0.021 (5)*
H2W2	0.714 (2)	0.7655 (19)	0.1444 (12)	0.032 (5)*

Table 3

Selected bond lengths (Å) for complex $(C_4H_{16}N_3)[Cu(NO_3)(C_2O_4)_2].2H_2O$.

Cu1—O3	1.9424 (8)	N2—H2N2	0.919 (9)
Cu1—O4	1.9436 (8)	N3—C4	1.4835 (15)
Cu1—O2	1.9441 (8)	N3—H3N3	0.905 (9)
Cu1—O1	1.9497 (8)	N3—H2N3	0.897 (9)
Cu1—O5	2.4229 (9)	N3—H1N3	0.901 (9)
O1—C5	1.2769 (13)	N1—C1	1.4816 (14)
O4—C8	1.2741 (13)	N1—H1N1	0.896 (9)
O2—C6	1.2823 (13)	N1—H2N1	0.907 (9)
O3—C7	1.2806 (13)	N1—H3N1	0.898 (9)
O6—C5	1.2353 (14)	N4—O11	1.2321 (15)
O9—C8	1.2410 (13)	C7—C8	1.5500 (15)
O7—C6	1.2344 (13)	C5—C6	1.5463 (15)
O8—C7	1.2341 (14)	C3—C4	1.5190 (16)
O5—N4	1.2727 (13)	C3—H3A	0.940 (16)
O1W—H1W1	0.891 (15)	C3—H3B	0.952 (17)
O1W—H2W1	0.911 (16)	C4—H4A	0.936 (18)
O2W—H1W2	0.910 (15)	C4—H4B	0.936 (19)
O2W—H2W2	0.867 (15)	C2—C1	1.5201 (16)
O10—N4	1.2494 (14)	C2—H2B	0.964 (16)
N2—C2	1.4906 (14)	C2—H2A	0.984 (18)
N2—C3	1.4915 (15)	C1—H1A	0.982 (17)
N2—H1N2	0.906 (9)	C1—H1B	0.950 (17)

O3—Cu1—O4	85.68 (3)	O10—N4—O5	119.69 (10)
O3—Cu1—O2	92.72 (3)	O8—C7—O3	126.11 (10)
O4—Cu1—O2	178.39 (3)	O8—C7—C8	118.79 (10)
O3—Cu1—O1	172.77 (4)	O3—C7—C8	115.10 (9)
O4—Cu1—O1	96.30 (3)	O6—C5—O1	126.75 (10)
O2—Cu1—O1	85.25 (3)	O6—C5—C6	118.02 (10)
O3—Cu1—O5	97.33 (3)	O1—C5—C6	115.20 (9)
O4—Cu1—O5	85.42 (3)	O9—C8—O4	125.77 (10)

O2—Cu1—O5	95.05 (3)	O9—C8—C7	118.71 (10)
O1—Cu1—O5	89.77 (3)	O4—C8—C7	115.52 (9)
C5—O1—Cu1	111.67 (7)	O7—C6—O2	125.21 (10)
C8—O4—Cu1	111.58 (7)	O7—C6—C5	119.74 (9)
C6—O2—Cu1	112.05 (7)	O2—C6—C5	115.03 (9)
C7—O3—Cu1	111.52 (7)	N2—C3—C4	107.70 (9)
N4—O5—Cu1	114.78 (7)	N2—C3—H3A	108.2 (10)
H1W1—O1W—H2W1	106 (2)	C4—C3—H3A	111.1 (9)
H1W2—O2W—H2W2	109 (2)	N2—C3—H3B	109.8 (11)
C2—N2—C3	113.24 (9)	C4—C3—H3B	110.6 (10)
C2—N2—H1N2	108.4 (11)	H3A—C3—H3B	109.3 (14)
C3—N2—H1N2	108.8 (11)	N3—C4—C3	109.90 (9)
C2—N2—H2N2	110.1 (11)	N3—C4—H4A	108.5 (10)
C3—N2—H2N2	107.6 (11)	C3—C4—H4A	110.5 (10)
H1N2—N2—H2N2	108.6 (15)	N3—C4—H4B	107.9 (11)
C4—N3—H3N3	109.1 (12)	C3—C4—H4B	111.2 (11)
C4—N3—H2N3	110.7 (12)	H4A—C4—H4B	108.7 (15)
H3N3—N3—H2N3	107.6 (16)	N2—C2—C1	107.92 (9)
C4—N3—H1N3	112.2 (12)	N2—C2—H2B	109.1 (9)
H3N3—N3—H1N3	105.8 (16)	C1—C2—H2B	110.3 (9)
H2N3—N3—H1N3	111.3 (17)	N2—C2—H2A	107.1 (10)
C1—N1—H1N1	106.1 (11)	C1—C2—H2A	112.2 (10)
C1—N1—H2N1	110.4 (11)	H2B—C2—H2A	110.2 (14)
H1N1—N1—H2N1	112.0 (16)	N1—C1—C2	110.48 (9)
C1—N1—H3N1	107.6 (12)	N1—C1—H1A	107.4 (10)
H1N1—N1—H3N1	110.0 (16)	C2—C1—H1A	111.4 (10)
H2N1—N1—H3N1	110.6 (17)	N1—C1—H1B	105.3 (10)
O11—N4—O10	120.42 (11)	C2—C1—H1B	111.7 (10)
O11—N4—O5	119.86 (11)	H1A—C1—H1B	110.2 (14)

Cu1—O5—N4—O11	117.46 (13)	O3—C7—C8—O4	1.98 (14)
Cu1—O5—N4—O10	-60.53 (13)	Cu1—O2—C6—O7	177.32 (9)
Cu1—O3—C7—O8	174.54 (9)	Cu1—O2—C6—C5	-0.87 (11)
Cu1—O3—C7—C8	-6.70 (11)	O6—C5—C6—O7	7.18 (16)

Cu1—O1—C5—O6	172.36 (10)	O1—C5—C6—O7	-170.80 (10)
Cu1—O1—C5—C6	-9.86 (11)	O6—C5—C6—O2	-174.51 (10)
Cu1—O4—C8—O9	-176.16 (9)	O1—C5—C6—O2	7.50 (14)
Cu1—O4—C8—C7	3.87 (11)	C2—N2—C3—C4	179.07 (9)
O8—C7—C8—O9	0.86 (15)	N2—C3—C4—N3	-171.87 (9)
O3—C7—C8—O9	-177.99 (10)	C3—N2—C2—C1	174.28 (9)
O8—C7—C8—O4	-179.17 (10)	N2—C2—C1—N1	-176.58 (9)

Table 4

Hydrogen bonding network in the framework of complex $(C_4H_{16}N_3)[Cu(NO_3)(C_2O_4)_2].2H_2O$.

D—H···*A*	*D*—H	H···*A*	*D*···*A*	*D*—H···*A*
O1*W*—H1*W*1···O2*W*^{i}	0.89 (2)	1.91 (2)	2.7795 (14)	166 (2)
O1*W*—H2*W*1···O5^{ii}	0.91 (2)	2.02 (2)	2.8944 (13)	160 (2)
C4—H4*A*···O4^{ii}	0.936 (18)	2.594 (17)	3.3220 (14)	135.0 (14)
N2—H1*N*2···O2*W*^{ii}	0.91 (1)	1.92 (1)	2.7733 (13)	155 (2)
N1—H1*N*1···O7^{iii}	0.90 (1)	2.00 (1)	2.8080 (13)	150 (2)
N1—H2*N*1···O6	0.91 (1)	1.83 (1)	2.7215 (13)	169 (2)
N3—H3*N*3···O2^{iv}	0.91 (1)	1.97 (1)	2.8258 (13)	157 (2)
N2—H2*N*2···O1*W*	0.92 (1)	1.80 (1)	2.7128 (14)	170 (2)
C3—H3*B*···O11^{i}	0.952 (17)	2.584 (18)	3.5192 (17)	167.3 (15)
O2*W*—H1*W*2···O9	0.91 (2)	1.83 (2)	2.7236 (12)	168 (2)
N3—H2*N*3···O6^{v}	0.90 (1)	2.36 (2)	2.9461 (13)	123 (2)
N3—H2*N*3···O7^{v}	0.90 (1)	1.96 (1)	2.8184 (13)	159 (2)
N3—H1*N*3···O8^{vi}	0.90 (1)	1.94 (1)	2.8174 (13)	164 (2)
C2—H2*B*···O10^{i}	0.964 (16)	2.548 (16)	3.3939 (15)	146.5 (12)
C2—H2*A*···O10^{vi}	0.984 (18)	2.608 (18)	3.4958 (15)	150.1 (13)
N1—H3*N*1···O9^{i}	0.90 (1)	2.07 (1)	2.8445 (13)	144 (2)
N1—H3*N*1···O8^{i}	0.90 (1)	2.23 (2)	2.9493 (13)	136 (2)
O2*W*—H2*W*2···O3^{vii}	0.87 (2)	2.28 (2)	3.0685 (13)	151 (2)
O2*W*—H2*W*2···O10^{vii}	0.87 (2)	2.39 (2)	2.9656 (13)	125 (2)